An Investigation of the CSC-MIG Welding Process for Deposition of Conventional, Ultrafine and Nanostructured MMC Coatings

Patrick Vespa

Department of Mining and Materials Engineering
McGill University
Montreal, Canada
August 2010

A thesis submitted to the office of graduate studies and research in partial fulfillment of the requirements for the degree of master of engineering

Abstract

Welding based coating deposition techniques allow high rates of material deposition and form a permanent metallurgical bond between the coating and the substrate material. Welding based methods can also provide an economic alternative over other industrial coating deposition processes where high initial capital investment and running costs can be restrictive. As with all technological sectors, the need for new and improved machinery and processes to meet industrial needs provides a drive for continued research. The controlled short-circuit MIG (CSC-MIG) welding system is a newly developed welding apparatus built to overcome several shortcomings associated with traditional MIG welding. It allows for greater control of many welding parameters and has reduced heat input during deposition when compared with conventional MIG welding systems. This project was conducted to understand the CSC-MIG welding system as a process and as a hardfacing deposition technique through examination of the microstructural features and transformations of Ni/WC coatings.

Several coatings deposited with a Ni/WC electrode wire, with heat input ranging between 10 J/mm and 110 J/mm, were examined. It was found that the detrimental decarburization reactions acting on the WC particles, as seen in thermal spray systems, do not occur when welding with the CSC-MIG. Although the energy input during welding with the CSC-MIG system is significantly lower than for traditional MIG, dissolution of the reinforcing phase is an issue to be contended with and must be minimized through proper selection of welding parameters. Precipitation of a reaction layer around the WC/W_2C reinforcing phase was identified as WC; the average thickness of which increased from 3.8 μm to 7.2 μm for the low and high heat input condition, respectively. Precipitation of newly formed WC particles was also observed; their size distribution increased from D_{50} = 2.4 μm in the low heat input weldment to D_{50} = 6.75 μm in the high heat input weldment. The hardness of the deposited coatings decreased from 587 HV_{10} to 410 HV_{10} when the energy input was increased from 10.1 J/mm to 108.7 J/mm. Using a pre-placed powder method, as in submerged arc welding, several coatings were embedded with either conventional, ultrafine or nanostructured WC powder. In the analysis of these tests, it was found that the method of embedding the WC

particles into the coating had an effect on the overall dissolution of the reinforcing phase. Although the loss of the nanostructure was observed in coatings embedded with the nanostructured WC feedstock, the precipitation of ultrafine WC single crystals is likely to increase the wear resistance compared with conventional sized WC additions.

This thesis contains the first journal articles submitted for publication using results from experiments conducted with a CSC-MIG welding system.

Résumé

Les techniques de revêtement à base de soudage permettent de hauts niveaux de déposition et forment une liaison permanente entre le revêtement et le substrat. Les techniques basées sur le soudage peuvent aussi fournir une alternative économique aux autres méthodes de revêtements industriels où les coûts sont souvent plus élevés. Comme dans tous les secteurs technologiques, le besoin pour des solutions industrielles nouvelles et améliorées contribue au dynamisme pour la recherche continuelle. Le système de soudage par MIG aux courts-circuits contrôlés (CSC-MIG) est une machine récemment développée pour surmonter quelques points faibles du soudage MIG classique. Celui-ci permet un meilleur contrôle des paramètres de soudage et un débit de chaleur moins élevé en comparaison avec les systèmes de soudage MIG traditionnels. Ce projet a été réalisé afin de comprendre le système CSC-MIG en terme de processus et de technique de déposition de revêtement en examinant les caractéristiques et transformations des couches déposées avec un fil-électrode à base Ni/WC.

Plusieurs couches avec des apports énergétiques entre 10 J/mm et 110 J/mm furent examinées. Il a été démontré que la décarburation des particules de WC, qui caractérisent les revêtements obtenus par projection thermique, n'affecte pas les couches produites avec le CSC-MIG. Bien que les apports énergétiques avec le CSC-MIG soient réduits en comparaison avec le MIG traditionnel, la dissolution des particules de WC est un phénomène auquel on doit faire face tout en minimisant sa gravité en optant pour une sélection de paramètres de soudage appropriée. La précipitation d'une couche réactive à l'entour de la phase renforcent WC/W_2C a été identifiée comme étant du WC; l'épaisseur de cette phase a crû de 3.8 μm à 7.2 μm pour les conditions de soudage à basse et haute intensité respectivement. La précipitation de nouvelles particules de WC a également été observée; leur distribution de taille a augmenté de D_{50} = 2.4 μm pour la condition de soudage à basse intensité à D_{50} = 6.75 μm pour la condition de soudage à haute intensité. La dureté des revêtements a diminué de 587 HV_{10} à 410 HV_{10} lorsque l'apport énergétique a été accru de 10.1 J/mm à 108.7 J/mm. En utilisant une méthode de poudre pré-placée comme pour le soudage sous flux, il a été découvert que la méthode de mélange des particules de WC dans le revêtement a eu un effet sur la dissolution de la

phase de renforcement. Malgré que la nanostructure des revêtements faits avec la méthode de poudre pré-placée et ayant des particules nanostructurées ait été perdue, la précipitation de particules ultra-fines de monocrystal risque tout de même d'augmenter le niveau de résistance à l'usure en comparaison avec des revêtements provenant de particules conventionnelles.

Cette thèse contient les premiers articles à être soumis pour publication utilisant des résultats d'expériences avec le système CSC-MIG.

Acknowledgements

First I would like to thank my supervisor, Mathieu Brochu, for giving me the opportunity to explore the materials science field through this master's thesis and for his assistance and guidance throughout it all.

I am very grateful towards all the staff in the Materials Engineering department; especially Helen Campbell, Monique Rindeau, Robert Paquette, In-Ho Jung and Ray Langlois. Their support with my tests, experiments and lessons in theory is what made this master's thesis possible. I would also like to thank Barbara Hanley for her guidance throughout my journey as a student in Mining and Materials Engineering; this thesis would likely not have been handed in on time if it weren't for her.

I would like to thank Phil, Cory, Dom, Jason, David, Dave, Ramona, Graeme, Alex, Bamidele, Rabab, Abdul, Ahmad, Yaneth, Cesar, Sergio and Sonia for furthering my understanding of materials science, for the generosity of their time and willingness to assist me in my various experiments, for the great conversations, laughs and work breaks. A special thanks to Gustavo for all his help and dedication to the project throughout summer/fall 2009.

Thanks to everyone who contributed to the Blades of Steel becoming the B-league Intramural Champions in 2009 – 2010. Having a crowd of 50^{+} materials engineering students and friends cheering you on can make miracles happen! I am happy to say that I walk away from McGill knowing that Mathieu's wish ("I want that cup!") has come true!

Finally, I would like to thank my family, especially my parents, Barbara and Sesto, my sister, Alisa, and my brother, Geremi, for their support and encouragement toward realizing my dreams and ambitions. Thanks Dad and Germ for your comments and suggestions with this thesis!

Contribution of Co-Authors

The author of this thesis is the primary author in all papers included in this thesis. Prof. Mathieu Brochu was the supervisor of the author's Masters of Engineering program and is included as co-author. Philip T. Pinard is included as co-author in recognition for his SEM work including EDS and EBSD mapping. Prof. Raynald Gauvin is included as co-author in recognition of his help in understanding of the EBSD technique and for providing access to microscopes capable of analyzing the WC-based phases.

Table of Contents

List of Figures

List of Tables

Chapter 1. Introduction

Materials science and materials engineering involves exploring the relationships between the structures and properties of materials. With this knowledge, materials engineers can design the makeup of a material to generate a desired set of properties. However, research is not always founded on the generation of novel materials but is also focused on the creation of new solutions to old problems in a more economical fashion. In order to achieve this, it is often useful to combine the properties of two separate materials into one. This can be achieved through the production of metal matrix composites (MMCs). A MMC is a metallic phase material with a second phase added to enhance or add a desired mechanical or physical characteristic. MMC research began when materials development was favored for military applications but it was only in the 1980's that research and development for other purposes began. The application of these materials became important in many industrial sectors but especially in auto and rail transportation systems, thermal management and aerospace industries. In the last 20 years, MMCs have become materials of extensive interest from a technological and commercial standpoint. The development of wear resistant MMC coatings has the potential to reduce expenditures by minimizing the damage caused by wear and corrosion of mechanical parts and materials in many industrial sectors. Although there are currently many types of MMC coating deposition methods, research continues to find innovative techniques which are more cost effective, efficient and which surpass the limitations of older approaches.

1.1 Welding

Joining techniques were among the first manufacturing technologies ever created; beginning in ancient cultures to makes tools and weapons. However, joining techniques in the 21st century have become even more important to society. So important in fact that practically every manufactured good uses some type of joining technique [1]. These techniques include, but are not limited to, mechanical fasteners, attachments, bonding, cements, mortars, welding, brazing, soldering and more. In modern times, welding has

dominated from an economic stand point and it has been projected that greater than half of the gross national product of all industrialized nations stems directly or indirectly from the joining technique [1]. Welding can be described as the coalescence of two metals or non-metals through heating, with or without the application of pressure, or by applying pressure alone, with or without the use of a filler material, to achieve atomic bonding between the elements. In a more wide-ranging definition, welding is any process which causes materials to join through the attractive action of interatomic or intermolecular forces [1, 2, 3].

1.1.1 Gas metal arc welding

Several different welding techniques available in industry are outlined in Table 1. One of the most widely used is Gas Metal Arc Welding (GMAW). It is commonly referred to as MIG (Metal Inert Gas). As a process, it has been around since the early 20th century yet was only commercially available in the 1950s [4]. MIG welding was initially limited by high cost, consumable wire electrodes, relatively crude wire-feeding systems and power sources that were not well suited to this type of welding. It was primarily used for welding aluminum and stainless steel [4]. Today, GMAW is the preferred type of fusion joining for most industrial applications due to its versatility and the numerous advantages it presents over other techniques. The advantages of GMAW include [4, 5]:

1) It is the only consumable electrode welding process that can be used for welding all commercial metals and alloys
2) Welding can be performed at any angle/position
3) High metal deposition rates
4) High quality welds at high speeds
5) Longer welds can be achieved due to the continuous wire feed

Table 1: Different types of fusion welding available in industry. [6]

Group	Welding Process	Group	Welding Process
Arc welding	Carbon arc	Oxyfuel gas welding	Oxyacetylene welding
	Electrogas		Oxyhydrogen welding
	Flux-cored arc		Air acetylene welding
	Gas metal arc		Pressure gas welding
	Gas tungsten arc	Resistance welding	Flash welding
	Plasma arc		Projection welding
	Shielded metal arc		Resistance seam welding
	Stud arc		Resistance spot welding
	Submerged arc		Upset welding
Solid-state welding	Cold welding	Other welding processes	Electron beam
	Diffusion welding		Electroslag
	Explosion welding		Flow
	Forge welding		Induction
	Friction welding		Laser beam
	Hot pressure welding		Percussion
	Roll welding		Thermit
	Ultrasonic welding		

1.1.1.1 Principles of operation of GMAW

Gas metal arc welding is an arc welding process that joins metals together by heating them by means of an electric arc formed and maintained between a continuously fed metal electrode wire filler and the work piece [6, 7]. Shielding of the arc and the molten weld pool is achieved by an externally supplied inert gas or inert gas mixture such as argon and/or helium [6, 7, 8]. A schematic illustration of GMAW process can be seen in Figure 1.

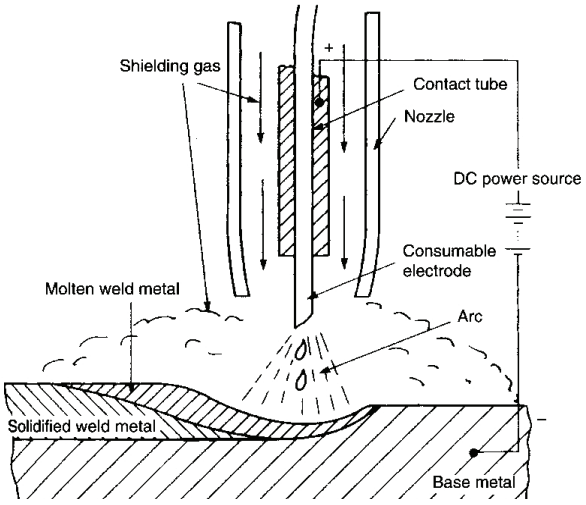

Figure 1: Schematic diagram of GMAW process. [1]

The electric arc produces the necessary heat required to melt the filler metal. Molten metal in the form of droplets are then deposited in one of several transfer modes onto the base metal into what is called the weld pool [6]. Globular, spray and short-circuiting are the three predominant transfer modes recognized in GMAW.

1.1.1.2 Globular transfer

As seen in Figure 2, globular transfer mode is characterized by the formation of large droplets at the tip of the electrode which subsequently release and fall to the work piece under the force of gravity. Given that gravitational forces dominate globular transfer, this deposition method has limited use. In addition, deposition rates are generally low and are influenced by the diameter of the consumable electrode [2].

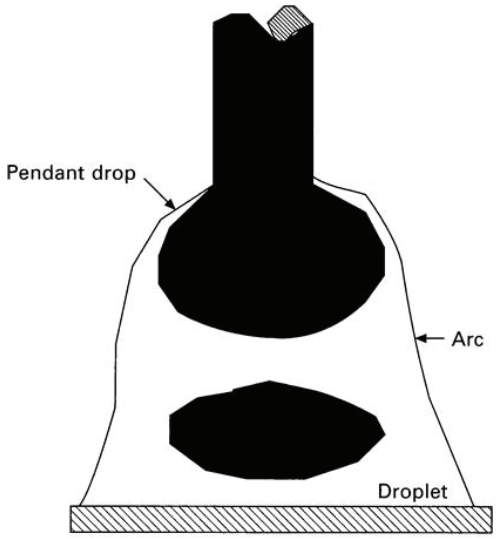

Figure 2: Schematic diagram of globular transfer mode in GMAW. [2]

1.1.1.3 Spray transfer

As the current in globular transfer is increased a threshold called the spray transition current is passed which changes the deposition mode from globular to spray [2, 9]. This threshold varies with shielding gas, is proportional to the liquid metal surface tension and inversely proportional to the diameter of the electrode wire [5]. Spray

transfer is characterized by an axial transfer of fine, molten droplets deposited at rates of up to several hundred per second [1]. An argon or argon-rich shielding gas must be used in this transfer mode, if carbone dioxide gas is used, a globular to spray transition will not occur [6]. Figure 3 shows a schematic of the spray transfer deposition process. Spray transfer is an attractive option since it is less likely to produce spatter and has a high deposition-rate when downhand welding. Furthermore, it has been found that the droplets are actually projected axially through the arc with force, this allows spray transfer to be used in any welding position [2, 5]. Unfortunately, the minimum current for spray mode is sometimes too high for certain materials [10].

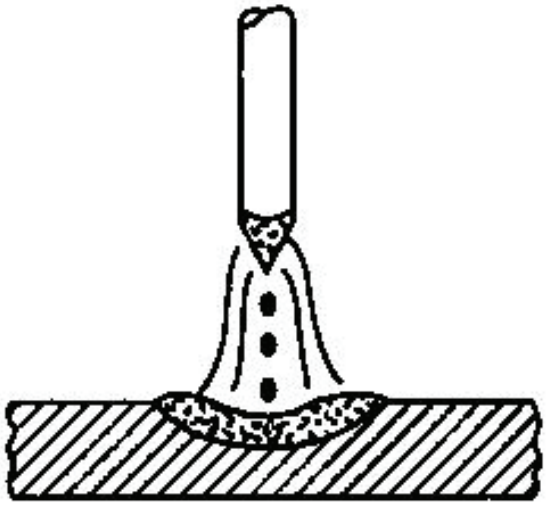

Figure 3: Schematic diagram of spray transfer deposition. [6]

1.1.1.4 Short-circuit transfer

In short-circuiting transfer, droplets formed do not flow across the arc gap as they do in globular and spray transfer but rather they form at the end of the electrode wire and are then deposited by inserting the electrode wire into the weld pool [1, 8]. The rate at which the drops are transferred to the weld pool can vary from anywhere between 20 and 200 Hz [6]. Short-circuit transfer method is characterized by the ability to produce a fast-freezing weld pool, which is sought-after for welding thin sections [7, 8]. It must also be

noted that depositions of this type penetrate less than with spray transfer. A depiction of the deposition mode and its four process stages is shown in Figure 4.

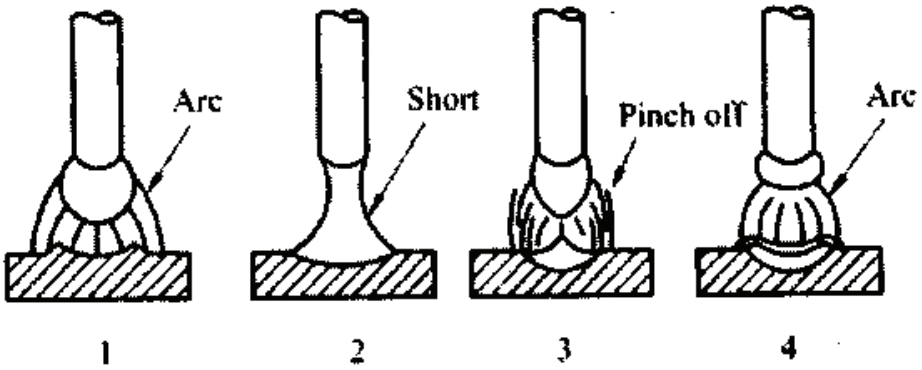

Figure 4: **Diagram of GMAW short-circuit transfer mode. [6]**

A characteristic of this type of deposition technique is mean welding currents lower than in globular and spray transfer modes. Consequently, this lowers the total heat input to the bead which can be favorable during solidification of the weld pool. A schematic of the current and voltage waveform at various points during the welding process is depicted in Figure 5. At position 1, the arc is well established, the voltage is high and the current is low; this point denotes the end of the portion of the cycle where heat is generated to melt the electrode wire. As soon as the molten tip of the electrode touches the weld pool a short circuit is created, the voltage drops and the current begins rapidly increasing from position 2 until position 3. Once the droplet is deposited, contact between the electrode wire and the weld pool is lost and the arc reforms (position 4). At this point the voltage increases rapidly and the current begins to drop. As the droplet on the end of the electrode begins to reform with heat from the arc, the voltage diminishes as well as the current and the process is repeated again.

It is known that this cyclic process can be fairly unstable and produce a substantial amount of spatter [11]. It is for this reason that several current rise and fall sections are controlled by adjusting the inductance in the power source [6].

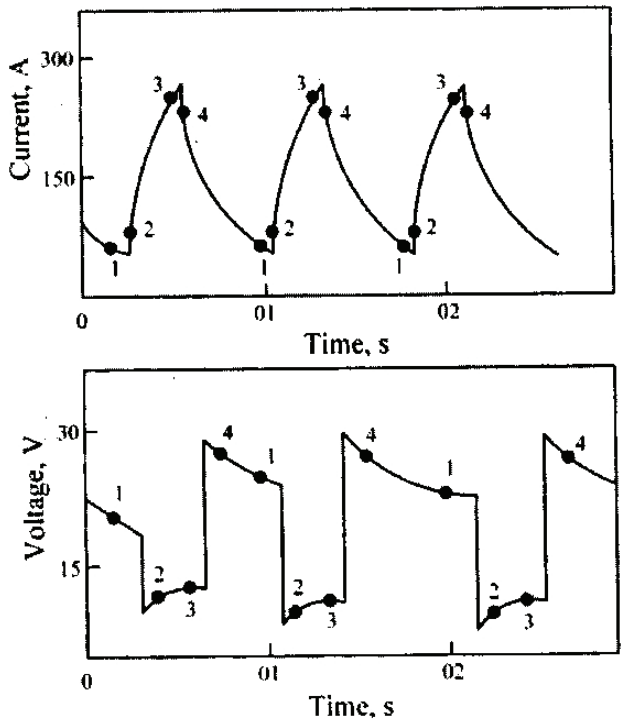

Figure 5: **Current and voltage waveform at various points during short-circuit welding. [6]**

1.1.1.5 Pulsed transfer

Pulsed transfer (GMAW-P) is not a metal transfer process in itself, it is a controlled form of spray welding [12]. It was developed to allow spray-type transfer to occur at average currents below the spray transition current [2]. This is achieved by maintaining a low level background current with periodical injections of high current pulses which allow the metal to be transferred [10, 12]. Figure 6 is a basic representation of a current-time diagram during pulsed welding.

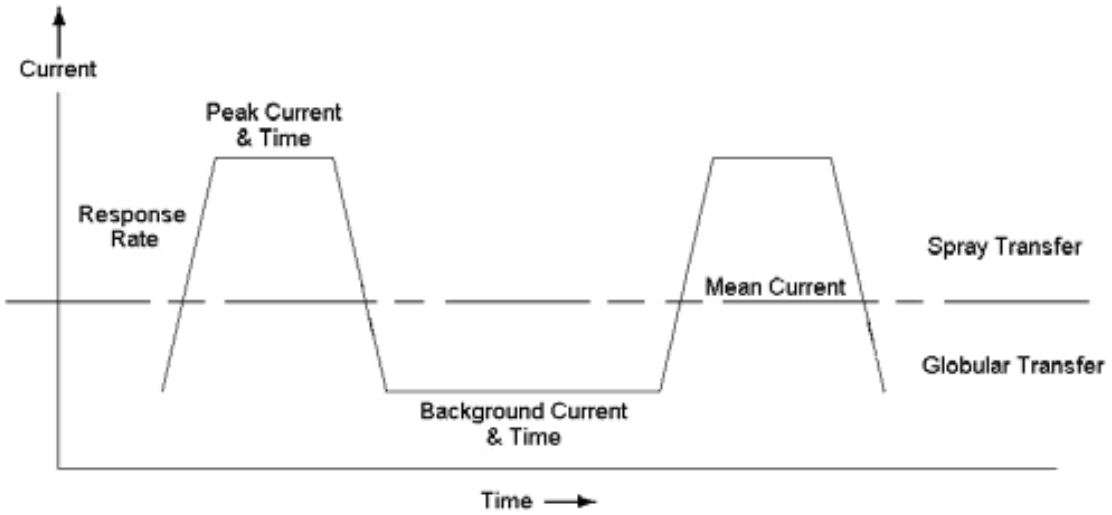

Figure 6: **Basic representation of a current-time diagram of pulsed welding. [10]**

The primary parameters to be controlled are the peak current, background current, background current duration, peak current duration and the pulsing frequency.

The main advantage of pulsed transfer is that it reduces the overall heat input to the weld making it available to be used with a wide range of materials yet achieves the fusion depths associated with spray transfer. In addition, when proper welding parameters are chosen, it has been noted that tensile, impact and fatigue properties of the weld joint in some steels have been enhanced [13]. The GMAW-P technique also reduces spatter [12].

The disadvantages of pulsed transfer are associated with the difficulty of choosing proper welding conditions (peak current, peak time, etc.) and is the primary reason that pulsed transfer has not been favored in industry [12]. Improper selection of pulsing parameters can result in a varying number of drops per pulse which consequently yields poor weld quality [14]. The difficulty associated with selecting the right parameters in GMAW-P has spurred much investigation into the development of methods to better determine the conditions that will provide higher weld quality.

1.1.2 CSC-MIG welding

Examination of the short circuit MIG welding stages has led to a better understanding of the fundamentals of the process [15, 16]. The Controlled Short Circuiting (CSC)-MIG welding system is a welding apparatus developed in the late 1990s to overcome several shortcomings associated with traditional MIG welding [17]. It was created in order to avoid problems with material transfer in order to obtain increased process stability [15, 17]. The CSC-MIG system works in conjunction with a process control system and a fast reacting wire feed unit to modulate the electrodes wire's position and speed depending on which process phase it is in [17].

The CSC-MIG process is subdivided into four phases [17].

1) Arc phase 1: The arc ignites and the electrode wire is retracted to the desired arc length (also known as the top dead center position).

2) Arc phase 2: From the top dead center position, the ignited electrode wire is fed down towards the basematerial until the molten droplet makes contact with the weld pool and a short circuit is created.

3) Short Circuit phase 1: As soon as the short circuit is detected by the system, the wire feed unit decelerates the electrode wire until it comes to a stop at the bottom dead center position.

4) Short Circuit phase 2: From bottom dead center, the wire is then retracted until the liquid connection between the end of the electrode wire and the weld pool has been broken. At this point the cycle begins again.

The process control system allows the user to control wire feed speed, wire retraction speed, arc length, current level during arc phase and short phase and several other process parameters. Other advantages of the CSC-MIG welding system include a virtually spatter free welding process as well as a reduction in the energy input during deposition [18].

.

1.1.3 Heat input

The material science behind welding is extremely complex as the processes occur under non-equilibrium conditions and involve mechanical, thermal, chemical and possibly electrical phenomena [1]. A large quantity of research has been conducted into the effects of heat input on the weld and its immediate surroundings.

Above a certain temperature the heat input from the arc causes the base material to undergo changes in state (e.g., from solid to liquid) and structure (e.g., microstructure). For certain materials these changes can be quite significant and often involve mechanisms such as metal, gas-liquid chemical reactions, solidification, grain growth, recrystallization, polymorphic or allotropic solid state transformations and more. The changes that ultimately occur depend on several characteristics including the base material, the filler wire, the level of heating, shielding gas, and rates of heating and cooling [1].

Several factors need to be considered to control the heat input during welding. The main factors are:

1) The heating rate. This is particularity important at the point of energy deposition as it gives rise to thermally induced local stresses and strains.
2) The time at peak temperature. This is important because all reactions take a certain amount of time to occur i.e., dissolution of gases from the atmosphere into the molten metal.
3) The rate of cooling after the heat has been removed. This is important as the phase transformation temperatures of materials change depending on the cooling rate. The phase transformation temperatures can shift which may lead to either desirable or undesirable crystal structures in the weldment [1].

The net energy input (H) into the weld can be calculated based on the following formula:

$$H = (\eta E I) / R \qquad [5, 7]$$

Where I = current (A)

E = voltage (V)

R = travel velocity (mm/s)

η = efficiency factor of welding method

Typically of GMAW, the welding efficiency factor is between 0.66 – 0.85 while other welding processes are usually lower (e.g., between 0.21 and 0.48 for GTAW) [5].

Lou and Kou [19] performed experiments to better understand the sources of heat transfer in welding and to estimate the proportion of heat transfer from each source. Their studies looked at the arc, filler metal droplets and cathode heating to the base metal in GMAW of aluminum. They found that within the range of the power inputs they studied (0 – 6 kW) 45 % of the heat input came from the arc, 25 % from the droplets and 10 % from cathode heating. The remaining 20 % of the power input were lost to the environment. These result can be used to help reduce heat inputs when welding.

1.1.4 Heat flow

The formula to describe heat flow in a weldment as a function of time is [20]:

$$\frac{\partial}{\partial x}\left(k(T)\frac{\partial T}{\partial x}\right)+\frac{\partial}{\partial y}\left(k(T)\frac{\partial T}{\partial y}\right)+\frac{\partial}{\partial z}\left(k(T)\frac{\partial T}{\partial z}\right)+\dot{Q}=\rho C_p(T)\frac{\partial T}{\partial t}$$

where:

x = coordinate in the welding direction (mm)

y = coordinate transverse to the welding direction (mm)

z = coordinate normal to the weldment surface (mm)

T = the temperature in the weldment (K)

k(T) = thermal conductivity of the metal (J/mm s K) as a function of temperature

ρ(T) = density of the metal (g/mm^3) as a function of temperature

C_p(T) = specific heat of the metal (J/g K) as function of temperature

Q = rate of internal heat generation (W/mm^3)

This general equation can be solved for one, two or three dimensions depending on the type and accuracy of analysis needed. The more dimensions which are included the more complex the solution becomes. In the 1940's, Rosenthal used certain steady-

state assumptions to simplify the mathematical equation of heat flow during welding. Rosenthal made these assumptions to derive a useful analytical solution [20]:

1) Steady-state heat flow
2) Point heat source
3) Constant thermal properties
4) Negligible heat of fusion
5) No heat losses from the workpiece
6) No convection in the weld pool

Rosenthal's two-dimensional equation for welding thin sheets of infinite width is [20]:

$$\frac{2\pi(T-T_0)kg}{Q} = \exp\left(\frac{Vx}{2\alpha}\right)K_0\left(\frac{Vr}{2\alpha}\right)$$

Where:

T = temperature

T_0 = workpiece temperature before welding

k = workpiece thermal conductivity

g = thickness of the workpiece

Q = heat transferred from the heat source to the workpiece

V = travel speed

α = workpiece thermal diffusivity

= k/ρC where ρ and C are density and specific heat of the workpiece, respectively

K_0 = modified Bessel function of the second kind and zero order

r = radial distance from the origin

Rosenthal's three-dimensional equation for welding a semi-infinite workpiece is [20]:

$$\frac{2\pi(T-T_0)kR}{Q} = \exp\left[\frac{-V(R-x)}{2\alpha}\right]$$

Both these formulas can be used to calculate the temperature T{(x,y) or (x,y,z)} at any given point in the workpiece with respect to the moving heat source.

Since Rosenthal's equations were developed, numerous modifications have been made to suit specific needs. However, the general form is still in use today.

1.1.5 Solidification and cooling rates

The solidification processes of crystalline solids, alloys and all other materials involve complex mechanics that lead to the formation of favorable or unfavorable microstructures [1]. It is possible to control the microstructure obtained in GMAW by the control of heat input, solidification and cooling rates. This can be achieved by carefully selecting welding parameters and ensuring certain physical welding bead characteristics are met.

An example which shows the importance of possessing proper physical characteristics in a weld is the shape and size of the weld pool. Both these characteristics affect the heat input to the weld pool and consequently the mechanisms and kinetics of solidification as well as the cooling rate of the weldment. When the weld pool has the shape of a falling droplet, high thermally induced tensile stresses will be formed in the tail edge of the weld which can result in cracking [21]. Elliptical-shaped weld pools with a convex bead shape are less susceptible to cracking [8, 22]. Figure 7 shows the heat distribution in base metal during a single pass in GMA welding.

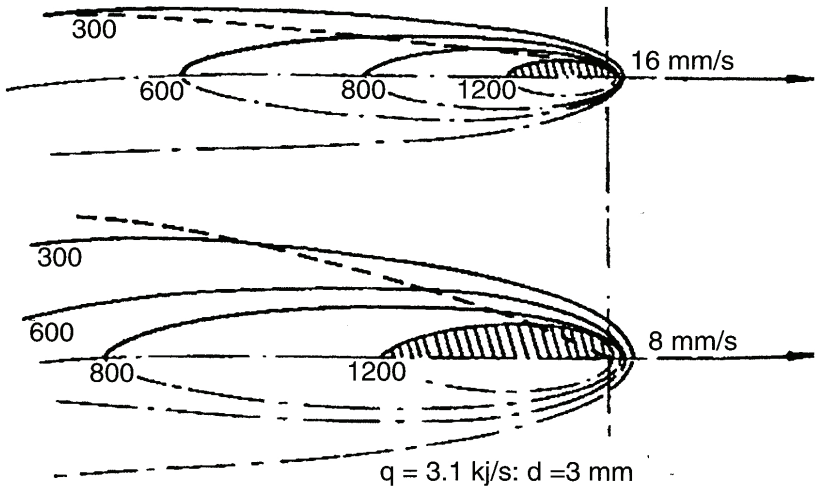

Figure 7: **Schematic diagram of the temperature distribution with different welding speeds. Heat input (q) = 3.1 kJ/s and plate thickness (d) = 3mm. [1]**

Welding speed is one of many parameters in GMAW which control the microstructure of the weldment. Other parameters such as the electrode wire feed speed, welding speed, arc length, penetration delay, voltage and current also need to be optimized to obtain solidification and cooling rates which result in desirable weld properties.

Better control of solidification and weld deposit properties have been obtained through the use of pulsed-GMAW as compared with traditional GMAW. Pulsing reduces the heat build-up, improves control of the size and shape of the weld bead and also improves arc stability [23]. Furthermore, the solidification mechanisms through pulsed GMAW are different than those from regular GMAW. The intermittent injection of heat into the weld pool allows solidification to take place during the pulse-off time period and during the development of a weld spot resulting from the next pulse. This allows for better control over the size of the heat affected zone (HAZ) as GMAW-P can produce a variety of welding transfer energy levels, deposit rates and resulting thermal cycles.

1.1.5.1 Solidification rate

As previously stated, solidification rates in welding are very important as it has a dramatic effect on the growth mode and size of grains in the final microstructure of the weld. Solidification rate (s) can be calculated using [5]:

$$S_t = \frac{LH_{net}}{2\pi k\rho C(T_m - T_0)^2}$$

where:

C, k, ρ are constants

T_m = metal temperature (˚C)

T_0 = ambient temperature (˚C)

L = latent heat of fusion (J/mm^3)

k = thermal conductivity of base material (J/m s K)

S_t = time between the beginning and end of solidification(s)

1.1.5.2 Cooling rate

The cooling rate in welding is also very important because it determines the final metallurgical structure of the fusion zone (FZ), partially melted zone (PMZ) and HAZ. The cooling rate also determines which transformations occur in the weldment and which phases will remain in the solidified material. The cooling rate (in ˚K/sec) for thin plates can be calculated using [1]:

$$\mathbf{R = 2\Pi k\rho C\ (h/H_{net})^2\ (T_c - T_0)^2}$$

where:

C, k, ρ are constants

T_c = temperature (K) at that point in the HAZ

h = thickness of the base material (mm)

ρ = density of the material (g/mm^3)

C = specific heat of the base material (J/g K)

1.2 Surface wear

The interaction between two mating surfaces can result in loss of material from the points of contact. The process by which surfaces in contact undergo loss of material is known as wear [24]. This phenomenon affects a wide range of components such as: railway lines, cutting knives, earth scoops, pump housings, agricultural plows, machine tools, mineral processing equipment, engines and automotive parts, heat exchangers, furnace components, food processing components, etc. Wear reduces the life of mechanical components in almost every sector of industry and leads to premature part replacement and increased production costs. Damage to materials through corrosion and wear cost the United States – by way of example, hundreds of billions of dollars on an annual basis [25]. Given the high costs associated with wear, much research has been conducted to develop protection against wear and extend the working life of components.

The surface properties of a material such as the microstructural features, surface energy, morphology, composition and hardness are the main factors which affect wear properties and largely determine its ability to resist wear [24].

1.2.1 Microstructural features

Microstructural features which appear on the surface of a material depend on the materials composition, the cooling rate and post-solidification processing [24]. Features such as grains and grain boundaries, their shape, size and type determine both the strength and toughness properties of a material [24]. Finer grains enhance strength and toughness properties, equiaxed grains result in isotropic properties and single grains result in directional properties [24].

Multiphase alloys and ceramics are more commonly used for wear-resistant applications [24]. Good examples are the different grades of steel. Various alloying elements are added to steels to enhance the physical, corrosion and wear properties and to provide materials with specific mechanical properties. In steels, the strength and hardness of the microstructure increase from pearlite to upper bainite to lower bainite and finally martensite. Although hardness is usually the best indicator of wear resistance, there are always exceptions to the rule. For example, wear-resistance in railway rails is

based on the microstructure and not the hardness and composition. The most widely used steel in railway rails corresponds to a eutectoid composition of 0.8% C and with a fully pearlitic microstructure. The reason for this is that dry sliding tests have confirmed that wear on pearlitic microstructure is lower than that of bainite or martensite, even though they are harder [26].

1.2.2 Surface composition

The chemical composition of a material plays an equally important role in surface wear [24]. Surface deposition techniques rely mostly on altering the surface chemistry by diffusing additional elements into the layer or by the addition of a separate wear resistant layer [24, 27, 28, 29, 30, 31, 32].

1.2.3 Surface hardness

The three main methods for determining the hardness of a material are the Vickers, Brinell and Rockwell indentation techniques. These techniques involve applying a known load to the surface of a material and then determine the hardness by measuring the area or depth of the resulting impression. Although several phenomenon play a role in wear, the easiest to measure and most indicative property of wear resistance is the surface hardness [33]. Research on carbide based composites has shown that the higher the hardness the less the wear volume will be [33, 34, 35].

1.3 Wear-resistant materials

A large variety of materials are available to prevent material loss due to wear. They can be divided into three major categories; metals, plastics and ceramics [24]. Another group used for similar applications are composites materials; they are a combination of two or more different types of materials whose properties combine together in a single material.

1.3.1 Metallic materials

There are a plethora of metallic materials to reduce wear in industry today. They include: steels, cast irons, cobalt alloys, nickel alloys, copper alloys, various thermal spray metallic materials and special metallic materials (such as: intermetallics and shape memory alloys) [24]. Metallic materials are quite often difficult to form into desired shapes while others are often too expensive for common applications [24]. On the other hand, they are very favorable for wear reduction because there are so many different alloys that can be produced to satisfy the majority of industry needs.

1.3.2 Polymeric materials

Another group of materials that are used for wear resistance are polymeric materials (i.e. plastics). The use of these types of materials provide advantages such as low cost, low density, good formability and good impact resistance when compared with metals and ceramics [24]. However, their main disadvantage are that they must be used at low temperatures, they possess low hardness and therefore do not resist wear very effectively [24].

1.3.3 Ceramics

Ceramic materials are interesting as they retain hardness at high temperatures, are chemically inert to various solutions and possess good thermal and electrical insulating properties [24]. They are used in applications involving extreme environments such as: high load, high speed, high temperature and highly corrosive environments [36]. For example, heat resistant ceramic oxides, including aluminia, titania and zirconia are used as heat resistant coating materials on engine exhaust valves and piston crowns [24]. The fact that they retain their hardness at elevated temperatures makes them ideal candidates to be used in cutting tools, automotive engines, jet engine burner nozzles and turbine blades [24].

Ceramic materials only show limited plastic deformation at room temperature and do not possess good toughness properties [36]. Consequently, bulk ceramic materials are

not ideal candidates for engineering applications where wear resistance is needed. In this case a combination of a ceramic and a more ductile metallic material is preferred. The combination of a ceramic and a metal is called a cermet and falls into the group of materials called composites.

1.3.4 Composites

Composite materials have been used to make a wide variety of structural parts in engineering applications. This is due to the fact that they possess a wide range of favorable characteristics such as: high strength, high stiffness, lightweight, good fatigue resistance, good corrosion resistance and excellent wear resistance [37, 38]. Composite materials are used to meet demanding material requirements throughout industry. For example, the largest airplane in the world as of 2008, the Airbus 380, has more than 50 % of its structure made of composite materials [38]. The composite materials used for the Airbus 380 offer a strength to weight ratio that no ceramic or metal has been able to match. Composites are also used to reduce material wear in industries such as farming, mining and automotive.

1.3.5 Cermets

Material design using cermets can take advantage of properties from both materials to provide an advantage over either individually. Although many types of MMCs exist in industry, one of the most common combines the ceramic, tungsten carbide (WC), with metallic nickel or cobalt. The addition of tungsten carbide (WC) powder particles within a metallic binder material is a widespread practice used in industry to increase the wear resistance of MMC coatings. In this composite, the ceramic provides the wear resistance while the metal, called the matrix or binder material, provides ductility and toughness and fixes the ceramic in place. WC is often favored over other carbides because of its high hardness, wear resistance and wettability by other metals [34, 39, 40]. The main function of the binder material is to have a sintering temperature lower than the decomposition temperature of the hard material so as to fix it in place and yield high toughness [24].

Research aimed at developing wear resistant materials and coatings to improve those currently in use can have significant economic benefits. The overall effectiveness of MMC coatings are determined by many factors including: type of carbide [28, 41], particle size, shape and grain size of the reinforcing phase [42, 43, 44, 45], volume fraction of matrix [32, 43, 46, 47], reinforcing phase structure [48], coating hardness [41, 49], solidification structures and phase characterization [50, 51, 52, 53, 54, 55], deposition parameters [32], wear properties [28, 44, 45, 47], carbide/matrix interface characteristics [41, 55], the presence of cracks and porosities [56] and the coating deposition technique.

1.4 Coating deposition techniques

Tungsten carbide based coatings are produced using a variety of surface modification techniques including: brazing [46, 55, 57], laser cladding [28, 32, 45, 53, 58], welding based methods [39, 41, 44, 59] and various thermal spray technologies. Much research is focused on improving these deposition techniques through analysis of deposition rates, energy input during deposition, ease of application as well as the characteristics mentioned in section 1.3.4.1. The method of depositing WC coatings has an effect on the overall coating effectiveness.

1.4.1 Thermal spray coatings

The production of WC based thermal spray coatings involves feeding a pre-alloyed powder at a controlled rate into the hot zone of a flame or plasma. The particles are rapidly heated to form partially or completely melted droplets and are then accelerated towards the substrate, with the impact forming a dense coating of agglomerated droplets [60]. One of the most widely applied thermal spray deposition techniques in industry is the high velocity oxygen fuel (HVOF) process [30, 42, 61]. Advantages of the HVOF process over other thermal spray systems include: higher particle velocities which favor coating bond strength, lower particle temperatures which reduces reactivity between alloying elements and shorter in-flight times reducing

exposure of the droplets to potentially harmful environments before impact [62]. Due to the fact that thermal spray processes form a mechanically bonded coating, they are characterized by a low bond strength between the coating splats and the coating/substrate material [46]. The lack of permanent metallurgical bond between splats can lead to chipping of the coating, removal of WC particles and premature breakdown of the wear resistant barrier [63]. One of the main drawbacks associated with thermal spray systems is decarburization of WC during spraying to form the brittle and less wear resistant W_2C phase [64]. This occurs when the WC and alloyed metal are heated with the spray flame, the WC can form new phases because of a loss of carbon by an oxidation reaction between the tungsten and the metallic phase present [64]. This reaction is detrimental to the WC reinforcing phase and is the reason that much research is conducted on the decarburization reaction [51, 52, 60]. Another disadvantage of thermal spray techniques is that they require large initial capital expenditure and can be quite costly to run [30, 65].

1.4.2 Arc-welded coatings

Arc-welded coatings are those which use heat generated by an electric arc to melt a metal or metal alloy which is then deposited on a substrate material and forms the surface coating [66]. This type of coating deposition technique is advantageous because it forms a strong metallurgical bond with the substrate material and has much higher deposition rates as compared with thermal spray systems [66]. In addition, welding based techniques require significantly less capital expenditure and have lower operational costs than do thermal spray techniques. The main drawback of arc-welding methods is that they involve high energy inputs which can induce significant residual stresses and deformations in the coating which can lower its wear resistance [46]. This high heat input can also cause dilution of the coating through base material dissolution which can alter the properties of the coating [46]. If the temperatures or the time in the molten state of the weld pool is too high or long, excessive dissolution of the reinforcing phase can occur, reducing the wear resistance of the reinforcing phase. This can lead to the formation of other carbide phases in the coating [64, 67]. As with all welding processes,

the study of the welding parameters is of critical importance as their modification can lessen or eliminate the negative impact of certain phenomenon [41, 59].

1.5 Nanomaterials

"Nanotechnology has been defined as being concerned with materials and systems whose structures and components exhibit novel and significantly improved physical, chemical and biological properties, phenomena and processes due to their nanoscale size" [68]. Nanoscale materials, or nanomaterials, are generally defined as materials with at least one dimension below 100 nm but larger than 1 nm [69]. This nanoscale dimension can relate to a coating thickness, a grain size, a particle diameter, the width of a conducting line or any particular attribute which may fall into this specific size category [70]. The uniqueness of their properties is largely attributed to the relatively large number of atoms positioned at the surface and interfaces. This creates materials which are highly dominated by surface effects and where surface energy plays an important role [68, 71]. Figure 8 exemplifies the relationship between the diameter of a palladium cluster and the number of atoms that exist at surface positions. The proportion changes dramatically from approximately 0 % at 630 nm to over 75 % at 1.2 nm. It is due to this extreme increase in proportion of surface atoms that nanomaterials have such incredibly different material properties compared with conventional materials. These changes include but are not limited to: increased strength/hardness, enhanced diffusivity, improved ductility/toughness, reduced density, reduced elastic modulus, higher electrical resistivity, increased specific heat, higher thermal expansion coefficient, lower thermal conductivity, and superior soft magnetic properties in comparison with conventional coarse-grained materials [68, 72]. It is because of these beneficial properties and their potential application in many industrial sectors that interest in nanomaterials is rising.

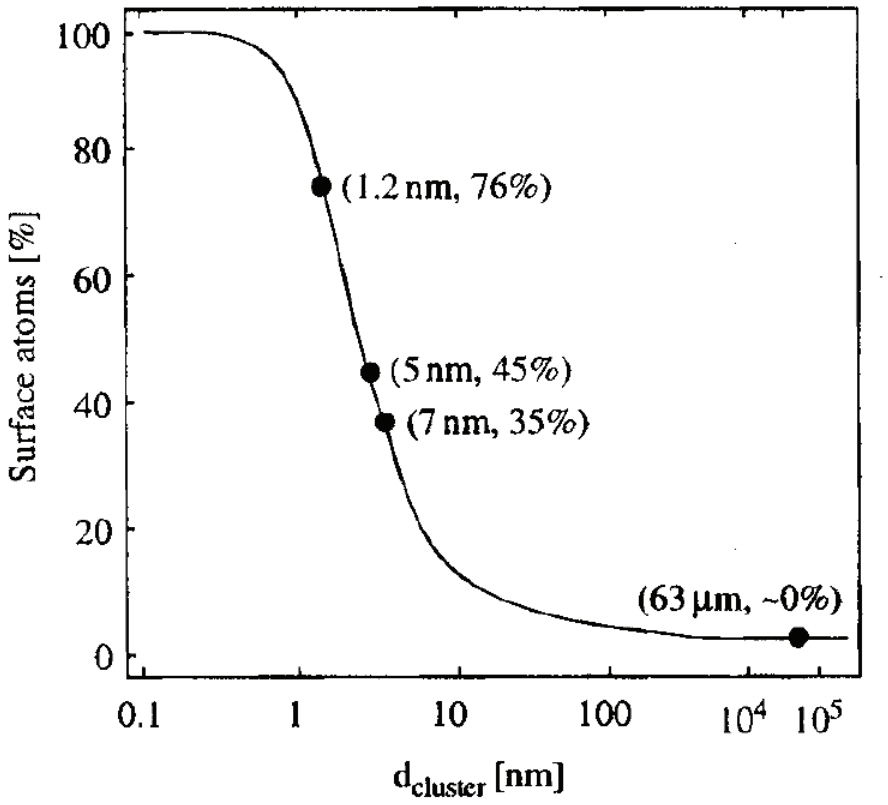

Figure 8: Proportion of surface atoms as a function of palladium cluster diameter. [68]

1.5.1 Nanostructured WC Coatings

One of the most notable property changes that occur when decreasing the grain size to the nanometric range is a 4 to 5 times increase in the strength and hardness when compared with crystalline materials [73]. It has been shown that the hardness of WC-Co composites containing nanoscale WC grains increases with volume fraction and decreasing grain size. The increase in hardness has been shown to accompany an increase in toughness. Since hardness is related to wear resistance, the abrasive wear resistance of nanostructured WC-Co is higher than microstructured WC-Co when compared at equal hardness [73]. Favorable results have also been achieved using certain coating deposition techniques. Research using nanocrystalline WC as feedstock in high velocity oxygen fuel (HVOF) and vacuum plasma spraying have produced coatings with higher hardness, better sliding wear behavior and corrosion resistance when compared with conventional WC feedstock [74, 75, 76]. Furthermore, the use of a mixture of

conventional and nanostructured cemented carbides in laser clad coatings has been shown to reduce wear rates over the use of either one individually [45]. As seen by example, coatings stand to benefit from the addition of nano-sized WC particles. The addition of these particles in MMC coatings has the potential to further increase its resistance to wear.

1.6 Research objectives

The main objective of this research is to investigate the CSC-MIG welding system as a Ni/WC coating deposition technique. To the best of the authors' knowledge, no previous work has been published on the CSC-MIG welding system or on its use as a coating deposition technique. Two journal articles, making up Chapters 2 and 3 of this manuscript have been written on the experiments performed.

The research featured in Chapter 2 was conducted to study the capabilities of the CSC-MIG welding system, its ability to deposit coatings using an industrial hardfacing electrode wire and to analyze, quantify and discuss microstructural features and transformations within the hardfacings.

The objective of Chapter 3 was to study the effects of the addition of conventional, ultrafine and nanostructured WC particles to the Ni based coatings using a pre-placed technique. This chapter explores the effect of the pre-placed technique on the dissolution/precipitation reactions in the MMC coatings.

Chapter 2. Analysis of WC/Ni Based Coatings Deposited by Controlled Short-Circuit MIG Welding

P. Vespa, P. T. Pinard, R. Gauvin and M. Brochu

Department of Mining and Materials Engineering, McGill University, 3610 University St., Montreal, Quebec, Canada H3A 2B2

2.1 Introduction

Coatings and coating deposition techniques are investigated because of the economic drive to reduce wear of materials in many industrial sectors [77]. Tungsten carbide (WC) is highly investigated as a reinforcing agent because it exhibits many desirable mechanical properties such as high hardness and superior wettability by molten metals compared with other carbides [53, 78, 79]. The WC powder particles act as the hard phase while the alloying elements form a ductile binder material; together they form a metal matrix composite (MMCs) and are used to significantly increase the wear life of industrial tools [28, 44, 45].

There are several methods available for the application of wear resistant WC coatings. One of the most widely applied thermal spray deposition techniques in industry is the high velocity oxygen fuel (HVOF) process [30, 42, 61]. One of the main drawbacks associated with HVOF is the decarburization of WC during spraying to form the brittle and less wear resistant W_2C phase [64]. Another disadvantage of thermal spray techniques is that there is not a permanent metallurgical bond formed between the individual hardfacing material splats or between the splats and the substrate. Consequently, a certain amount of porosity exists in the coating which, in addition to the lower intersplat strength, can lead to chipping, removal of WC particles and premature breakdown of the wear resistant barrier [63]. In addition, these techniques require large initial capital expenditure and can be quite costly to run [30, 65]. On account of these

shortcomings in the HVOF process, there is a need for alternative coating deposition techniques.

Compared with thermal spray techniques, welding based processes require significantly less capital expenditure and lower operating costs. In addition, they form a permanent metallurgical bond between the deposited material and the substrate. These advantages make them an interesting alternative to thermal spray processes. However, the main drawback of welding based hardfacing techniques is the high heat input required for deposition which favors excessive dissolution of the reinforcing phase.

Recent developments in Metal Inert Gas (MIG) welding techniques have allowed for better control of welding parameters and reduction of heat input during welding. A variation on the conventional MIG welding process allows for lower heat inputs and is thus attractive as a coating deposition technique which can reduce the dissolution of the reinforcing carbide phase. The Controlled Short-Circuit MIG (CSC-MIG) welding system is a welding apparatus developed in the late 1990s to overcome several shortcomings associated with traditional MIG welding [17]. Traditional MIG welding is known to have problems associated with material deposition and process stability [17]. The CSC-MIG operates in conjunction with a process control system and fast reacting wire feed unit to modulate the electrode wire's position and speed to obtain an extremely stable process in which spatter is nearly eliminated [13,15]. The CSC-MIG operates using the short-circuit deposition method and uses a control system that allows the user to set the arc length, arc time, current and several other welding parameters. Conventional MIG welding heat inputs range from 0.5 – 3.0 kJ/mm, while the CSC-MIG inputs 0.01 – 0.11 kJ/mm when using a WC/Ni-based hardfacing electrode wire [80, 81].

This research was conducted to study the features and transformations in the microstructure with heat input for WC/Ni based coatings deposited by the Controlled Short-Circuiting MIG welding system. Results on the microstructure evolution, phase formation, particle dissolution and coating hardness will be presented.

2.2 Materials and methods

Tests were conducted using the CSC-MIG welding system manufactured by Jetline Engineering. This system consists of two parts. The first is the WF-9829 MIG

torch assembly which contains an electrode wire drive system and torch. The second part is the 9829 CSC MIG weld process controller which uses a microprocessor to monitor and control the welding process parameters. The welder was mounted on a 3' by 3' Machitech CNC table with three translational degrees of freedom and the generator used to power the welding system was a Miller Electric XMT 350 CC/CV.

The welding tests were monitored using ARCAgent 3000P data acquisition system manufactured by IMPACT Welding. This system was used to monitor current, voltage and gas flow rate at a sampling frequency of 10 kHz. Heat input calculations provided by the monitoring system use the average instantaneous power of sampled data. This is regarded as the most accurate method of calculating heat input when current and voltage vary significantly with time [80, 82].

CSC-MIG welding parameters selection was based on visual inspection of cracking, discontinuity, repeatability and fusion to the basemetal. In addition, the use of the CSC-MIG process combined with the high-speed data acquisition system made it possible to achieve process stability by ensuring an even arc burning time and short-circuiting time and by the elimination of welding spatter [16].

A 1.6 mm cored electrode wire, PolyTung NiBWC, from Polymet Corporation was used to produce coatings. PolyTung NiBWC has a pure Ni sheath, is filled with a FeSiB powder and contains WC particles as a reinforcing agent. Full chemical composition of the cored electrode wire containing 38 – 45 wt.% WC particles, as stated by manufacturer, is shown in Table 2. Feedstock WC ranged between 45 – 200 μm in diameter with a mean particle diameter of 71 μm. The particle size distribution of the tungsten carbide, as determined with a Horiba LA-920 laser scattering particle size distribution analyzer, is shown in Figure 9. Figure 10 shows a micrograph of the WC powder, from which it can be seen that the feedstock is composed of angular particles.

In these experiments, single bead weld deposits were made in the flat position at a 90º angle to the substrate. Welding was carried out at 1 meter per minute (MPM) on plain carbon steel plates having dimensions 100 mm x 12 mm x 2.5 mm. The substrate was sandblasted to remove surface impurities prior to welding. A 75Ar –25CO_2 shielding gas was used and flowed between 36 – 37 cubic meters per hour (CMH) during

welding. Table 3 lists the CSC-MIG welding process parameters used for the reported experiments.

The samples produced were transversely cut using a Buehler Delta AbrasiMet abrasive cutter, mounted in Bakelite, ground with several steps of progressively finer SiC paper and polished with diamond suspensions up to a 1 μm finish. Optical micrographs of cross sections were taken with a Nikon Epiphot 200 with Clemex JS2000 image analysis system. Scanning electron microscopy (SEM) examination was performed using a JEOL JSM-840A and a Hitachi S-4700. Electron backscattered diffraction (EBSD) mapping was performed using a Nordlys II camera and the HKL Channel 5 software. The acquisition parameters were an accelerating voltage of 15 kV, an 8x8 image binning, a dwell time of 20 ms and a step size of 30 nm. No noise reduction technique was used. The phases used were Ni (space group: 225, a: 3.54 Å), WC (space group: 187, a: 2.91 Å, c: 2.84 Å) and W_2C (space group: 194, a: 2.98 Å, c: 4.71 Å). A Si(Li) detector and the Oxford Inca software were used for the energy dispersive spectroscopy (EDS) analysis. The acquisition parameters were an accelerating voltage of 15 kV, a processing time of 5 and a live time for the mapping of 2 hours. A Bruker D8 Discovery diffractometer using cobalt K_α X-rays at 40 kV and 0.002º step size was used for collecting x-ray diffraction (XRD) patterns. Hardness measurements were taken on a Buehler 5114 macro-vickers.

Table 2: Chemical composition of Ni-based, WC reinforced welding wire supplied by Polymet.

Chemical composition [wt.%]					
Si	B	Fe	C	W	Ni
0.81	1.06	0.7	2.81	41.02	Balance

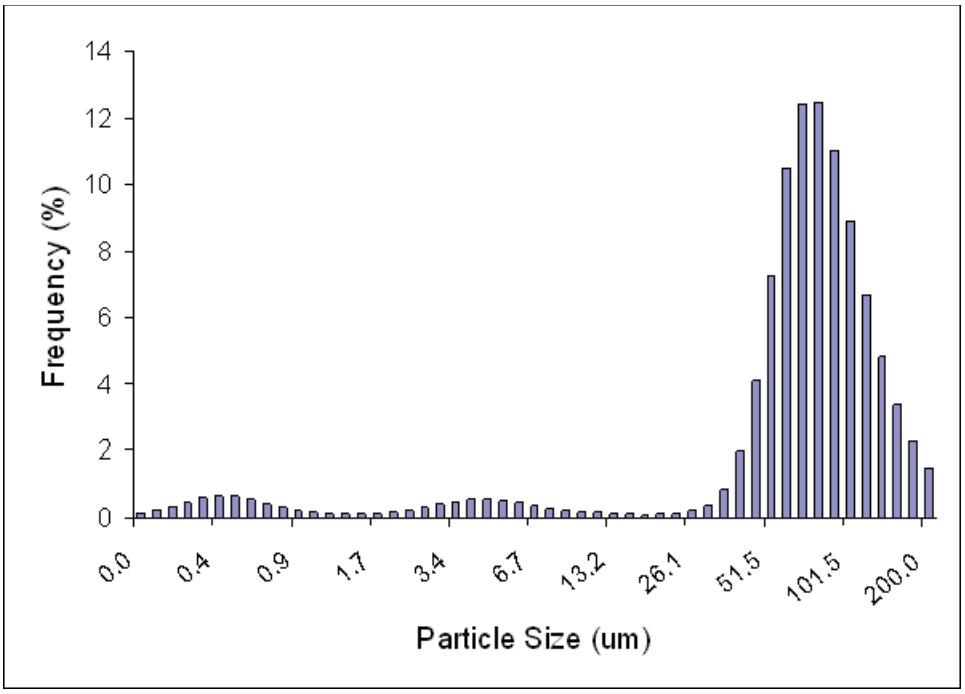

Figure 9: **Particle size distribution of the WC powder in the welding wire.**

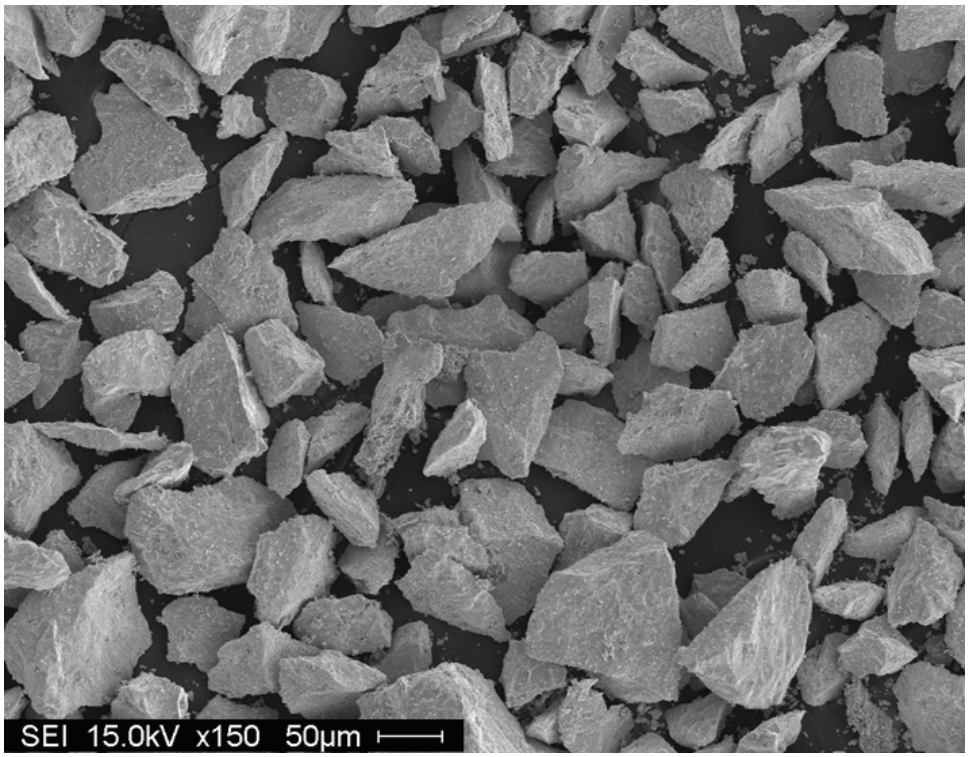

Figure 10: Micrograph of WC powder contained within the welding wire.

Table 3: CSC-MIG welding process parameters and energy input for the reported depositions.

Sample	A	B	C	D	E	F
Heat Input (J/mm)	10.1	17.3	22.7	38.9	11.7	108.7
Current Data						
Arc Time						
Initial arc current (A)	30	30	80	80	80	250
Time (ms)	7	7	7	7	7	7
Mid arc current (A)	30	100	80	160	80	250
Time (ms)	7	7	7	7	7	7
End arc current (A)	30	30	80	80	80	250
Short Circuit Time						
Start short current (A)	20	20	40	40	40	200
Time (ms)	7	7	7	7	7	7
Mid short current (A)	20	20	40	40	40	200
Time (ms)	7	7	7	7	7	7
End arc current (A)	20	20	40	40	40	200
Ramp Rates						
Rise (A/ms)	200	200	200	200	200	200
Fall (A/ms)	200	200	200	200	200	200
Wirefeed Data						
Down Wirefeed Speed (mpm)	5	5	8	6	6	12
Delay Before Wire Down (ms)	0	0	0	0	0	0
Up 1 Wirefeed Speed (mpm)	5	5	5	5	2	5
Delay Before Wire up (ms)	0	0	0	0	0	0
Up 2 Wirefeed Speed (mpm)	7	7	7	7	15	7
Arc Length (mm)	0.5	0.5	0.5	0.5	0.2	0.5
Penetration Delay (ms)	6	6	6	6	5	6
Start Sequence Data						
Preflow Time (s)	0.5	0.5	0.5	0.5	0.5	0.5
Runin Wirefeed Speed (mpm)	2	2	2	2	2	2
Process Starting Current (A)	60	60	60	60	60	60
Initial Arc Length (mm)	2	2	2	2	2	2
Preheat Current (A)	60	60	60	60	60	60
Preheat Time - Start Delay (ms)	50	50	50	50	50	50
Stop Sequence Data						
Stop Arc Length (mm)	1.4	1.4	1.4	1.4	1.4	1.4
Stop Time (ms)	40	40	40	40	40	40
Arc Stop Current (A)	40	40	40	40	40	40
Postflow Time (s)	0.3	0.3	0.3	0.3	0.3	0.3
System Data						
Max Arc Time (ms)	4000	4000	4000	4000	4000	4000
Burnfree Current (A)	0	0	0	0	0	0
Burnfree Delay Time (ms)	100	100	100	100	100	100
Burnfree Stop Time (ms)	984	984	984	984	984	984

2.3 Results and discussion

2.3.1 Characterization of welding electrode

The cored electrode wire consisted of an outer sheath made of Ni and a filler powder composed of WC/Si/Fe/B, as shown by XRD. Figure 11 shows the XRD pattern of the filler powder. From this, it can be seen that the tungsten carbide powder is composed of WC and W_2C. W_2C as a wear resistant material is undesirable as its mechanical properties are inferior to WC; it is more brittle and has been shown to exhibit lower chemical corrosion resistance [53, 64]. The presence of W_2C in the stock powder depends on the manufacturing process, these unwanted carbides can be formed in the production of tungsten carbide [83, 84]. Boron is used as an additive up to 25 at.% to reduce the melting point of the matrix while silicon is added as it has been shown to visibly increase the self-fluxing ability of the alloy [50]. When B and Si are added in conjunction with one another, they have been shown to deoxidize the substrate [32, 50].

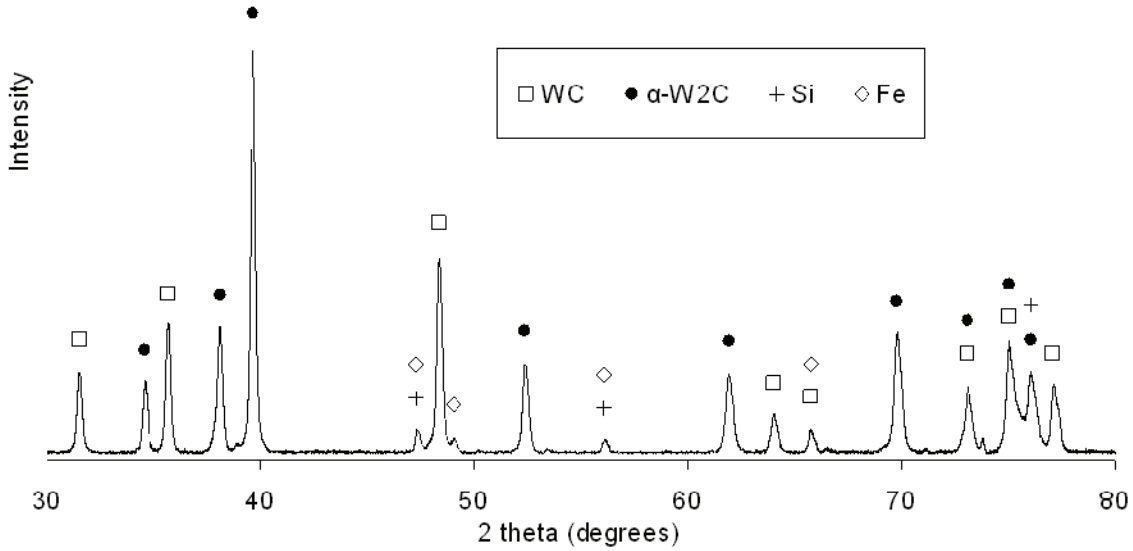

Figure 11: XRD pattern of electrode wire filler powder.

2.3.2 CSC-MIG welding current waveform

A portion of the current and voltage waveforms of sample A, B and E are shown in Figure 12a, b and c, respectively, to demonstrate the variability in obtainable waveforms with the CSC-MIG system. For comparison purposes, a waveform of traditional MIG welding is illustrated in Figure 12d. The system allows welding using a square waveform and has the capability to add a pulse in the short phase and/or the arc phase. The waveform of sample A, shown in Figure 12a, is a variation on the short-circuit welding waveform seen in traditional MIG welding (Figure 12d). A pulse in the arc phase was added in the waveform of sample B (Figure 12b). The addition of this pulse resulted in visibly increased fusion of the coating with the basemetal and an increase in heat input from 10.1 J/mm to 17.3 J/mm. Sample E (Figure 12c) was created to demonstrate how the CSC system can control the duration of the short circuit and arc phases. Note the increase in short-circuiting phase time and decrease in arc phase time as compared with Figure 12a.

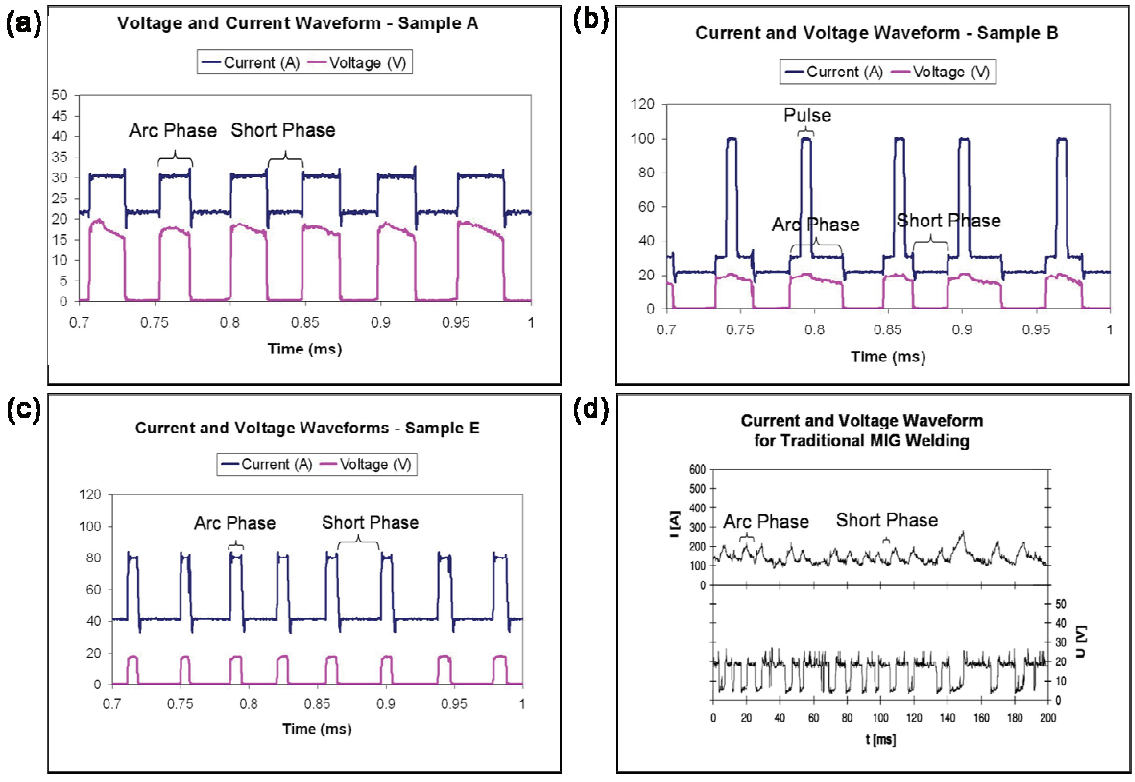

Figure 12: Current and voltage waveform as a function of time for: (a) sample A-having square waveform; (b) sample B-having square waveform with the addition of a pulse in the arc-phase; (c) sample E-having a lengthened time duration in the short-circuit phase and shortened duration in the arc-phase; (d) traditional MIG welding. [16]

2.3.3 Macrostructure and microstructure analysis and characterization

Two typical weldbead depositions are shown in Figure 13; a low heat input weldment (10.1 J/mm) in Figure 13a and a high heat input deposit (108.7 J/mm) in Figure 13b. Weldments are characterized by a continuous, uniform profile and are free from spatter. Initial analysis of the surface of the weldments shows some transverse cracking. When welding with hardfacing materials, cracking is to be expected. This is because of the high hardness and low ductility of the depositions which cannot accommodate the stresses generated during solidification and cooling [85]. The presence of transverse cracking is likely to reduce the wear resistance of the coating as it is a point from which chipping and spalling can initiate.

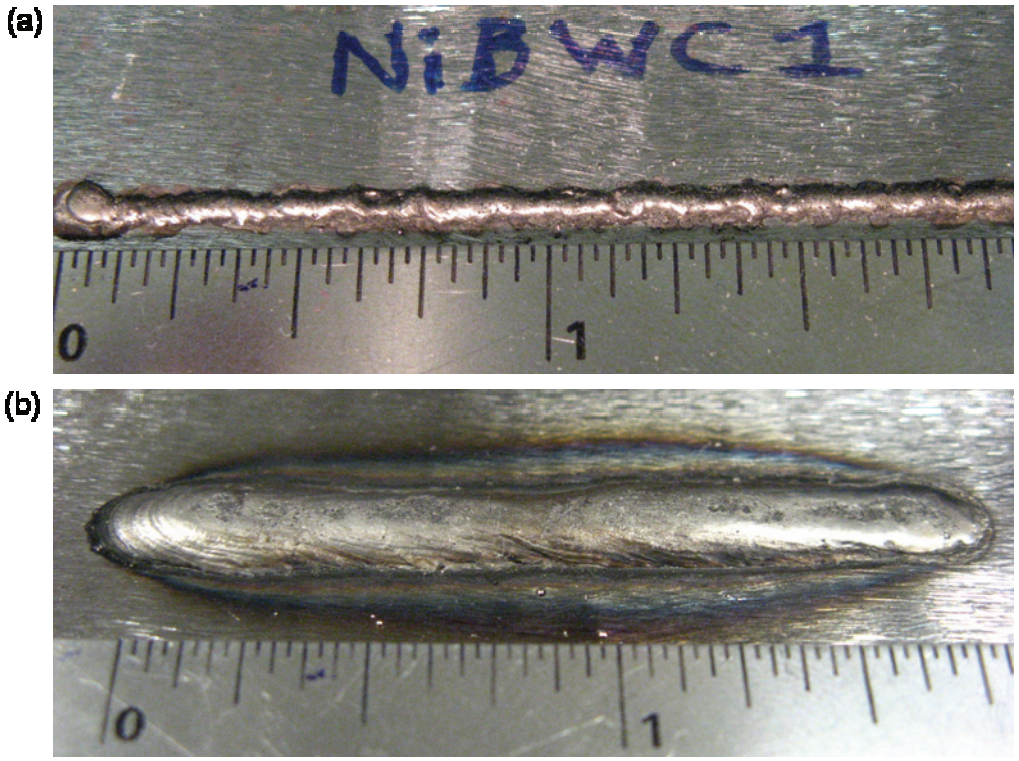

Figure 13: Beads produced with the CSC-MIG welding system using (a) low heat input parameters – sample A and (b) high heat input parameters – sample F.

Figure 14 shows the cross-section of six depositions made with the parameters outlined in Table 3. All coatings were metallurgically bonded with the substrate material although the lowest heat input deposition (sample A) did exhibit a small amount of

detachment from the basemetal. For this reason the heat input of sample A was considered as the lowest necessary to achieve adequate adhesion in these experiments. All depositions showed good dispersion of tungsten carbide throughout the matrix. Sample E contained 3.3 % porosity while the remaining samples contained between 0.04 - 0.6 % porosity. Average porosity level for sample A though F was 0.75 %.

The level of substrate dilution into the deposited coating can be defined as the ratio of the maximum depth of melted substrate to the sum of the maximum depth of melted substrate and maximum coating height [86]. Sample A through E, with heat input range 10.1 – 38.9 J/mm, show minimal amounts of substrate dilution (< 5 %). The highest heat input coating, sample F with 108.7 J/mm shows dilution ratio between 35 – 40 %. This is considered a high amount of dilution as the substrate material can cause a change in the material properties of the hardfacing. A dilution level of < 10 % has been proposed as acceptable levels for claddings [86].

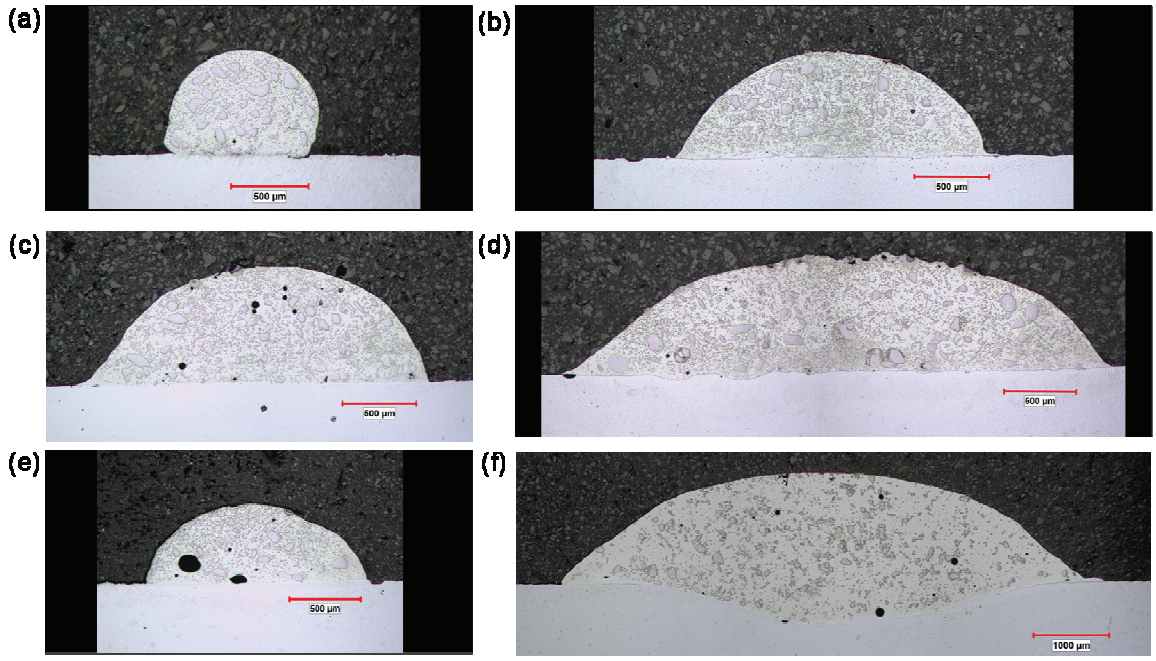

Figure 14: Cross sectional images of samples A to F. Hardfacings show good metallurgical bond with carbon steel substrate and small amounts of porosity.

The XRD patterns of sample A and F can be seen in Figure 15a and b, respectively. The phases corresponding to the x-ray diffraction patterns in the composite

coatings are outlined in Table 4. A few iron based compounds have been identified. Their presence originates from the reaction of the alloying elements with the 0.7 % Fe present in the electrode wire filler powder and significant dilution of the low carbon steel substrate. Given the level of Fe present and the longer molten state dwell time seen in sample F, ternary phases in the Fe-W-C system are likely to form [87]. This can explain the formation of the hexagonal η carbide, FeW_3C, in sample F which is not present in sample A.

Table 4: Potential phases in welding sample A and F based on X-Ray Diffraction data.

Welding condition	Heat input (J/mm)	Possible phases present based on XRD
A	10.1	WC, α-W_2C, C, FeNi, Ni_3B
F	108.7	WC, (Fe,C), B(Fe,Si), C, FeW_3C, FeNi, Ni_3B

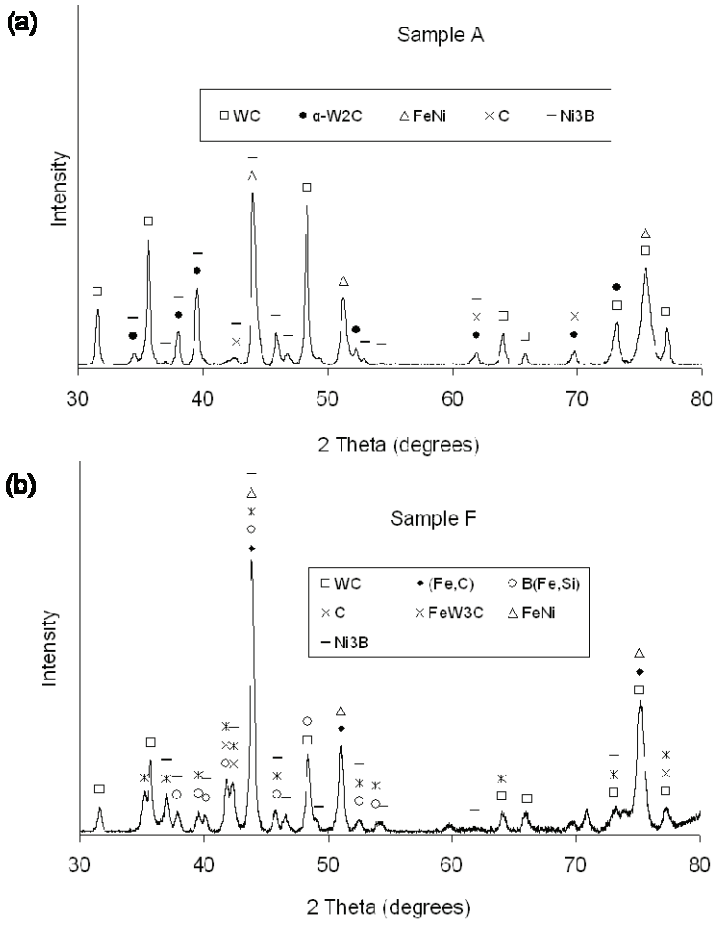

Figure 15: X-ray diffraction spectrum of the low heat input - sample A (a) and high heat input - sample F (b) depositions.

Typical backscatter electron images of the microstructure for the low and high heat input depositions are shown in Figure 16. Many authors have reported on the various phases that form between the WC and the alloying elements in the binder material [53, 54, 55, 88]. The compounds formed are thought to depend on the composition of the alloy and the solidification process [55]. In addition, longer dwell times in the molten state, as is the case for the high heat input deposition, have been shown to accelerate the formation of carbides [87]. In agreement with this, several morphological features characteristic of the high heat input deposition (Fig. 16b) are not present or are substantially less pervasive in the low heat input deposition (Fig. 16a). Two such features are the dendritic phase (marked as 1 in Fig. 16b) and the needle-shaped formations (marked as 2 in Fig. 16b) which can be seen throughout the matrix of sample F but not in sample A. A higher magnification image of the needle-shaped formations are shown in Figure 16d. Based on the XRD (Fig. 15b) and EDS analysis, they are thought to be FeW_3C.

A two phase system (marked as 3 in Figure 16a and b and shown clearly in Figure 16c) can be seen within the Ni matrix. As found by XRD analysis and commonly identified in other Ni-based MMCs with WC as a reinforcing agent, the dark phase likely corresponds to FeNi or Ni_3B [53, 54, 55, 56, 58]. The light coloured phase is dendritic and, as a result of the slower cooling rate, larger arm spacing characterizes sample F as compared with sample A. Although there was only one W-based phase identified (FeW_3C) in either sample A or F, EDS analysis reveals that the lighter coloured dendritic phase contains W. The W entered the matrix during the partial dissolution of the WC particles. The formation of a W-based phase is likely and is consistent with the fact that molten Ni dissolves WC rapidly, facilitating the formation of Ni - W - C liquid alloys [61]. It is possible that the W is forming a non-stoichiometric phase within the Ni matrix which causes a slight shift in position of the Ni peaks to lower Bragg angles.

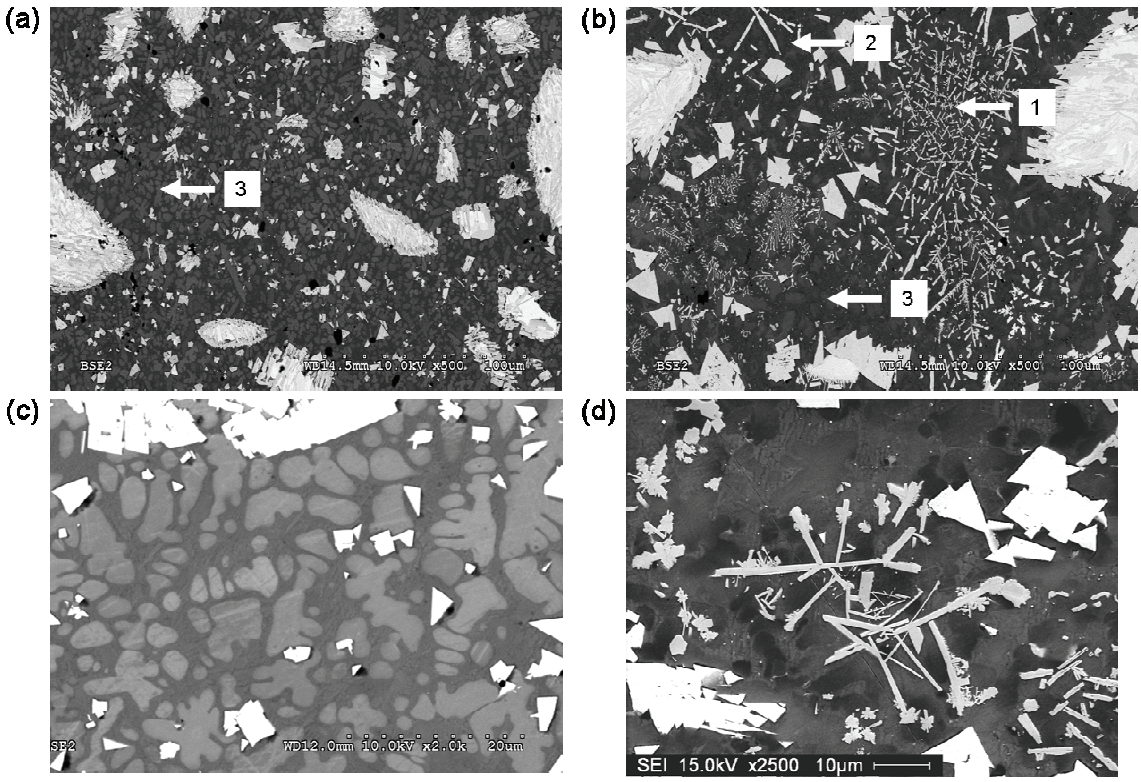

Figure 16: Typical cross-sectional images of Ni-alloy based hardfacings for low heat input (a) and high heat input (b) conditions. Higher magnification images clearly showing the two phase system within the matrix (c) of sample A and a needle-like/lamellar carbide (d) in sample F.

In the XRD pattern of the starting tungsten carbide powder (refer to Figure 11), the W_2C:WC ratio for the two largest peaks is greater than two. After welding, the XRD of the low heat input deposition (Fig. 15a) reveals that the W_2C:WC peak ratio diminishes to one-half in sample A. The XRD of sample F (Fig. 15b) shows that the WC phase is less present in the high heat input deposition when compared with the low energy input deposition. The W_2C phase is not found in the high heat input deposition. The diminishment of the relative occurrence of W_2C in the depositions made using the CSC-MIG is the reverse behavior of that which is observed in HVOF coating systems. HVOF research shows that the W_2C:WC ratio increases with decarburization [75]. The reduction in relative ratio of W_2C:WC with increasing heat input suggests that the CSC hardfacing process does not decarburize WC. On the other hand, a WC dissolution phenomenon is occurring.

To investigate the dissolution of the WC particles during welding, EDS mapping and EBSD was employed. Figure 17 shows an elemental map of a WC particle within

the Ni-based alloy matrix for sample E. Figure 17b, c and d depict the variations in C, Ni and W, respectively. The mapping shown in Figure 17b reveals that the core of the starting WC particles contains WC (darker phase) and W_2C (lighter phase), as depicted by the corresponding changes in C and W. A distinct reaction layer around the particles can be observed. Based on the mapping results, this layer seems to be composed of WC. To further infer the composition, EBSD was used to characterize the reaction layer. Figure 18a shows a SEM image of the area to be analyzed. Region marked A corresponds to the matrix; region B is the interfacial reaction layer and region C corresponds to the interior of the particle. Figure 18b shows the EBSD phase map of Ni (red), WC (blue) and W_2C (green). The core of the reinforcement is therefore composed of WC and W_2C while the reaction layer is indeed WC.

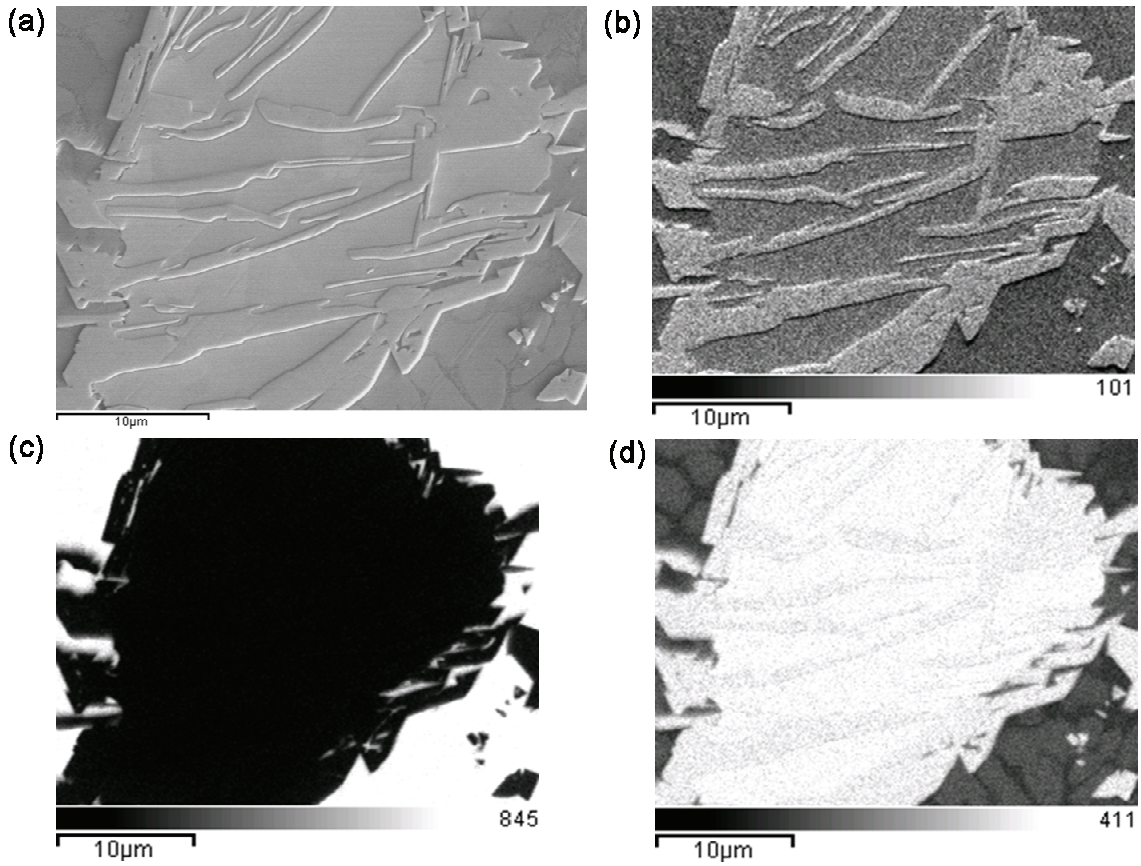

Figure 17: EDS mapping of Ni, C and W content in and around a tungsten carbide particle. The micrographs correspond to; (a) secondary electron image of WC/W_2C particle; (b) the variation of C content; (c) the variation of Ni content and; (d) the variation of W content.

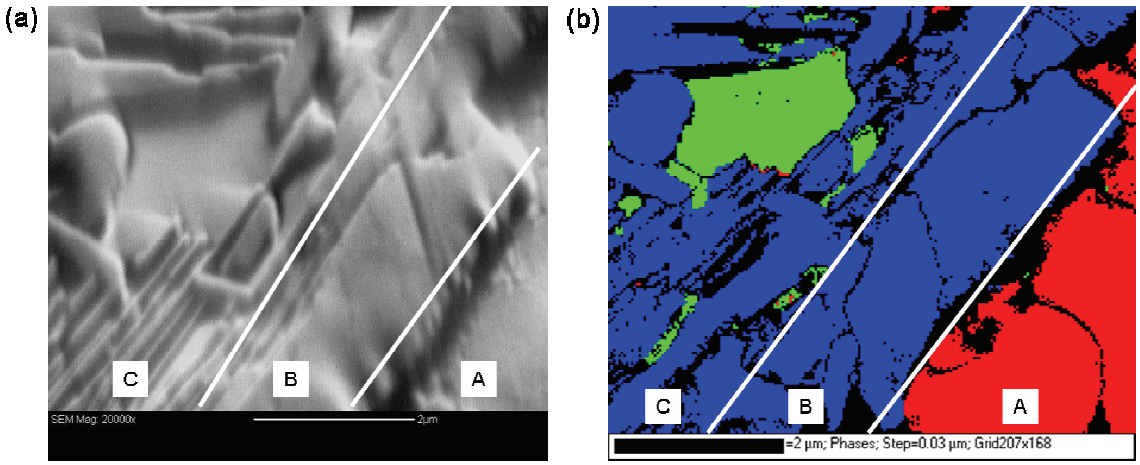

Figure 18: (a) Secondary electron SEM image taken at 15 kV of the interface region between a WC/W_2C particle and the matrix for identification by EBSD; (b) EBSD map of the phases present in the interface region. Three distinct phases can be seen: red represents the Ni matrix, blue represents the WC and green represents the W_2C.

In order to explain the formation of the WC reaction layer around the WC/W_2C reinforcing phase, the W – C binary system and isothermal Ni – W – C ternary phase diagrams have been analyzed. Given that welding is characterized by very high heating and cooling rates it cannot therefore be considered as an equilibrium process. Despite this fact, the phase transformations occurring can be better understood by considering the interactions between the main constituent elements of the weld pool at equilibrium conditions. A representative value for the droplet temperature in open arc welding deposition techniques, such as pulsed or spray transfer, has been establish at 2400°C [15]. Although short-circuit welding techniques have significantly lower droplet temperatures, a maximum weld pool temperature (peak temperature) of 2400°C has been used for the calculation of the ternary system using FactSage™ software. At the maximum weld pool temperature, the ternary phase diagram can be divided into two segments; a carbon rich and a carbon deficient segment. The carbon deficient segment contains two and three phase fields where γ-Ni is in equilibrium with W_2C and/or η carbides. Although Gustafson [89] did not include $M_{12}C$ carbide in his evaluation because they were not found to participate in solid/liquid equilibrium, $(Ni,W)_6C$ and $(Ni,W)_{12}C$ type carbides with FCC crystal structure have been reported to precipitate on solidification of the melt [27, 53]. The carbon rich segment is divided into three sections. With low concentration of W and C, γ-Ni alloy is in equilibrium. As the concentrations

of W and C increase, two phase field γ-Ni + $C_{(graphite)}$ and three phase field γ-Ni + $C_{(graphite)}$ + WC become thermodynamically stable. Given that WC and W_2C have low enthalpies of formation ($\Delta H_f°(WC) = -42.3 \pm 0.8$ kJ/mol, $T < 1575$ K and $\Delta H_f°(W_2C) = -30.5 \pm 1.3$ kJ/mol, $T > 1575$ K), WC and W_2C easily dissolve in the Ni-based weld pool [90]. Melting of the electrode wire followed by the dissolution of WC/W_2C reinforcing phase forms a Ni-based alloy solvent with low concentration of W and C solute. Mass transport of dissolved elements through fluid flow and short distance liquid phase diffusion produces a homogeneous distribution of W and C atoms in the matrix [53]. The XRD database used for peak analysis does not include any of the η carbides, however, referring to the XRD spectrum of Zhou et al. [27, 54] the peaks for M_6C and $M_{12}C$ type carbides align with the peaks from the XRD spectrum of sample A and F. It is therefore likely that upon solidification of the carbon deficient melt, η carbides are precipitated. Initial precipitation of M_6C and $M_{12}C$ type carbide shifts the carbon concentration to the carbon rich side of the Ni – W – C phase diagram. As the melt cools from peak temperature through final solidification in the C rich segment, there is precipitation of stable and metastable phases most of which are alloyed with Si, B, Fe found in the weld pool. At temperatures around 2000°C, γ-Ni + $C_{(graphite)}$ + WC is likely precipitated, followed by γ-Ni + WC (at 1500°C) which is subsequently followed by Ni + $C_{(graphite)}$ + WC (at 1000°C). It is suggested that the edges of the WC/W_2C reinforcing phase act as nucleation sites onto which the WC reaction layer heterogeneous precipitates during cooling of the weld pool. The continuity of the texture between the core particle and reaction layer shows evidence that the WC layer is produced by epitaxial precipitation.

2.3.4 Quantification of the tungsten carbide dissolution

Analysis of the tungsten carbide particle size distribution was performed prior to and after welding. This was achieved using a powder characterization technique which uses the projected area of the cross-section of a particle to determine the equivalent diameter of a sphere having cross-sectional area equal to the projected area. The equivalent spherical particle size diameter distributions for the stock WC powder as well as those for sample A and sample F are shown in Figure 19. As illustrated, the particle

size distributions for sample A and F have significantly shifted towards smaller particle sizes when compared to the starting WC feedstock. The high heat input on sample F and low heat input to sample A seemed to have no significant influence on the final particle size distribution. The statistical analysis of these distributions provide the results shown in Table 5. Using the equivalent spherical particle size diameter powder characterization technique, the stock tungsten carbide powder was determined to have an average particle diameter size of 99 μm with D_{50} = 95 μm. After welding, the average particle diameter dropped to 43 μm for both sample A and F. This reduction in average particle diameter was mirrored by the D_{50} values corresponding to 27 μm for sample A and 36 μm for sample F. The significant drop in average particle size and D_{50} is attributed to the dissolution phenomenon of the WC particles into the liquid matrix during welding. Another statistical approach for comparison of the WC particles before and after welding is the size distribution width, S_w. A high S_w value represents a narrow distribution while a low S_w value represents a wide spread of the particle size distribution. For WC, the S_w has a significantly lower value after welding. Prior to welding, the S_w for the WC particles was 6.5. After welding, the S_w decreased to 3 for sample A and 3.9 for sample F. The widening of the size distribution is again attributed to the thermal decomposition of WC particles. The largest WC particles – which have a relatively small surface area to volume ratio, remain large despite the heat input. On the other hand, most WC particles suffer significant dissolution which causes a shift in the particle size distribution to smaller particle diameters. The combination of the large particles largely unaffected by heat and the reduction in size of the smaller particles has the effect of widening the overall particle size distribution or lowering the value of S_w.

Table 5: Statistical analysis of the stock tungsten carbide powder and WC powder particles after welding for coating sample A and F.

Sample	Average (um)	D10 (um)	D50 (um)	D90 (um)	Sw (um/um)
Starting WC Powder	99	58	95	143	6.53
A	43	13	27	90	3.05
F	43	18	36	83	3.86

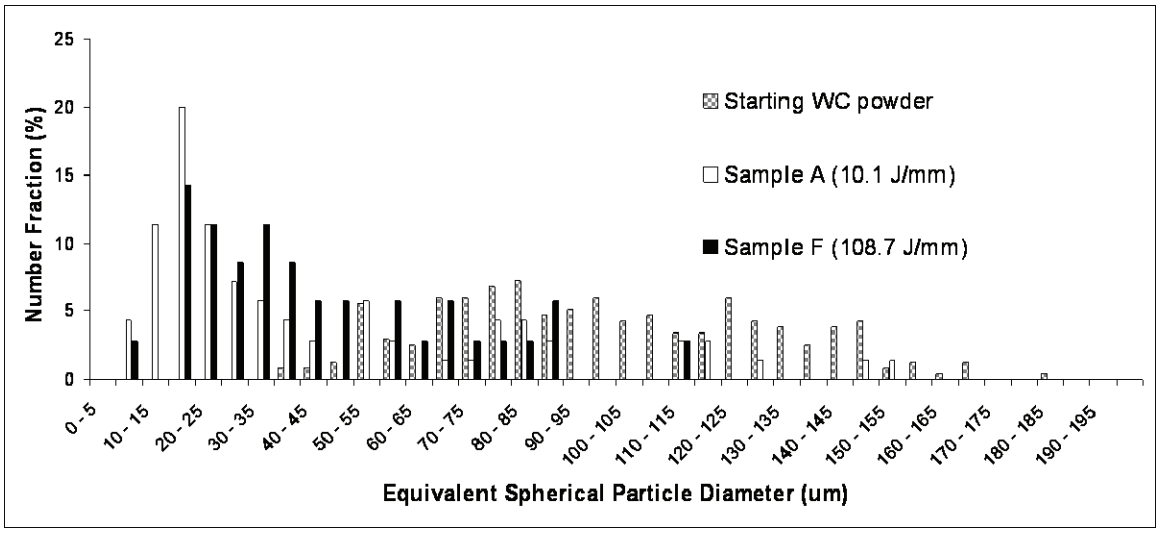

Figure 19: Graphical illustration of the particle size distributions for the starting WC powder before welding and for the high and low heat input conditions after welding.

Carbide dissolution is occurring during welding despite the fact that the CSC-MIG process has inherently lower heat input when compared with the conventional MIG process. The volume fraction of the WC coverage after welding was calculated by image analysis and the results indicate that the level of dilution increases with energy input. Comparing the extreme conditions, the low heat input, sample A, has a 25.2 ± 1.22 % volume fraction of reinforcing particles, while the high heat input, sample F, has a volume fraction reduced to 14.5 ± 0.56 %. The values obtained for the volume fraction of WC serve as an indication of the amount of tungsten carbide coverage in the coating. However, variation in the quantity of tungsten carbide per length of electrode wire is to be expected in the manufacturing process. It is for this reason that the standard deviation of the volume fraction can fluctuate from one cross section to another. The volume fraction of WC particles for the reported depositions is presented in Figure 20.

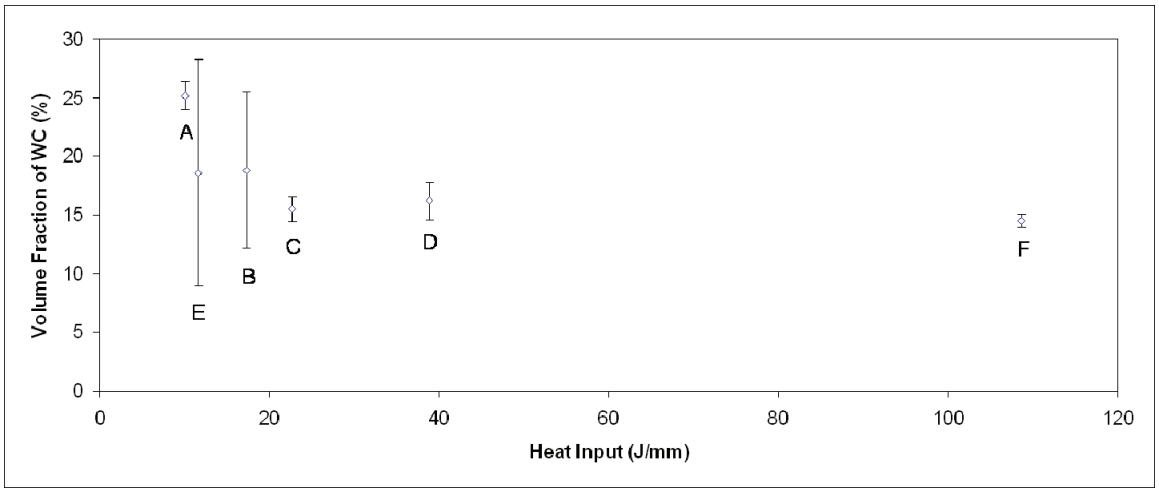

Figure 20: Volume fraction of tungsten carbide with heat input for samples A to F.

2.3.5 Quantification of the reaction layer formation around the WC particles

As demonstrated in section 3.3, a WC layer precipitated around the starting WC/W_2C reinforcing particles. The thickness of this layer for sample A through F is illustrated in Figure 21. Comparison of sample A and B shows the effect which the addition of a pulse in the arc phase has on the reaction layer thickness for two low energy input depositions. The addition of the pulse shifted the thickness of the reaction layer from an average value of 3.8 μm to 4.6 μm. A similar trend can be seen in the medium heat input deposition with a pulse (sample D) and without a pulse (sample C). The pulse shifted the average reaction layer thickness from 4.3 μm to 4.9 μm. Thus, it can be seen that the addition of a pulse slightly increases the reaction layer thickness for the same base waveform. A significant difference in the reaction layer thickness is found between the high and low heat input depositions, sample F and A, respectively. The extra 98.6 J/mm input to sample F shifted the average reaction layer thickness from 3.8 μm to 7.6 μm. The results indicate that the thickness of the WC reaction layer between the reinforcing phase and the matrix is more influenced by the energy input than by the presence of a pulse in the arc phase. In WC reinforced composite coatings, the carbide/matrix interface layer is partly responsible for the adhesion of the carbides to the matrix and influences the mechanical properties of the coating [32, 41, 46, 55]. Research suggests the presence of a reaction layer produces a higher bonding strength between the

WC particles and the Ni matrix and thus produces a coating with greater wear resistance [32, 55]. Although the reaction layer thickness increases with energy input, a larger reaction layer will not always produce a more wear resistant hardfacing. As the energy input during welding increases, other competing factors such as carbide thermal decomposition as well as basemetal dilution may lead to a reduction of the wear resistance [55]. Appropriate parameter selection is needed to establish a balance between competing phenomena.

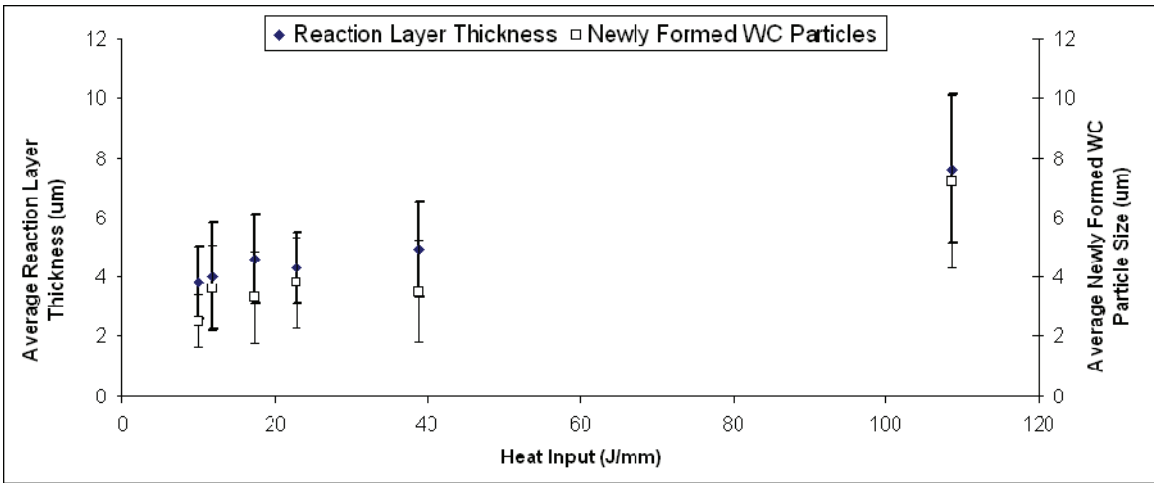

Figure 21: The effect of heat input on the WC layer thickness and size of newly formed WC particles.

2.3.6 Quantification of the newly formed WC particles

The newly formed WC particles precipitated in the Ni-based alloy matrix have been investigated by EBSD and analyzed for average size. These particles are important as they are a direct by-product of the dissolution of the original reinforcing phase. The EBSD experiments reveal that the newly formed WC particles are single crystals. SEM images of the original and precipitated particles can be seen in Figure 22. The average equivalent spherical particle diameter distribution of the newly formed WC particles for the reported hardfacings can be seen in Figure 21. The data shows no definite trends between the low heat input non-pulsed and pulsed waveforms or the medium heat input non-pulsed and pulsed depositions. This is likely due the similar quantity of WC particle dissolved during the welding for the low and medium energy input (see also Figure 20). On the other hand, a notable size difference between newly formed WC particles for the

high heat input and low heat input hardfacings is observed. The average particle size increased nearly three times from 2.5 μm to 7.2 μm. The increasing size of the particles is thought to be attributed to the higher quantity of WC dissolved and associated with the longer duration of the liquid melt pool. This could help in the formation of larger clusters in the liquid matrix that would reprecipitate as larger newly formed WC particles.

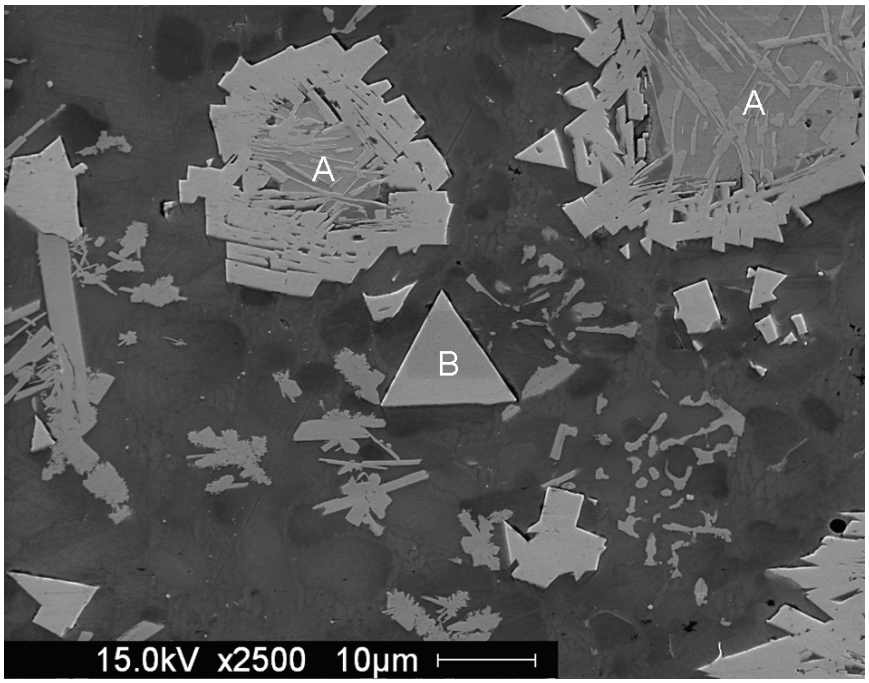

Figure 22: Backscatter electron images showing the original WC/W_2C particles with precipitated reaction layer (marked A) and the morphology of the newly formed WC particles (marked B).

2.3.7 Hardness of weldments

Microstructural features, surface composition and hardness are three principal factors which affect material wear properties [24]. The easiest to measure yet most indicative property of wear resistance is surface hardness and, as a general rule, the higher the hardness the higher the wear resistance [24, 30, 33]. For the measurement of surface hardness for materials with reinforcing particles, it is important to consider that the value obtained varies significantly with the fraction of reinforcing carbide to matrix ratio contained under the indent surface [34]. For this reason, it is important to choose an indent area that contains a representative proportion of matrix to reinforcing particle. The surface hardness of the low heat input coating, sample A, was 587 HV_{10} while that of the

high heat input coating, sample F, was 410 HV_{10}. The hardness measurements for samples A to F seem to indicate that the higher the heat input during deposition, the lower the hardness of the coating. The reduction in hardness with heat input can be attributed to several factors. Although the precipitation of the WC shell around the reinforcing particles increases with heat input, the rate of dissolution of the WC/W_2C carbides also increases with heat input. From the hardness measurement results, the potential benefits gained by the increase in WC reaction layer are offset by the increased levels of dilution. The dissolution of WC/W_2C particles increases the proportion of matrix to reinforcing phase and therefore reduces the overall hardness of the coating. Another factor affecting the hardness measurements among the samples is the increasing level of Fe intermixing from base metal dilution with increasing energy input. It is likely that the increasing level of Fe in the matrix has caused a loss of hardness of the coatings [34]. Furthermore, a longer dwell time in the molten state accelerates the formation of secondary and brittle carbides. Figure 23 shows the hardness of coating samples A through F.

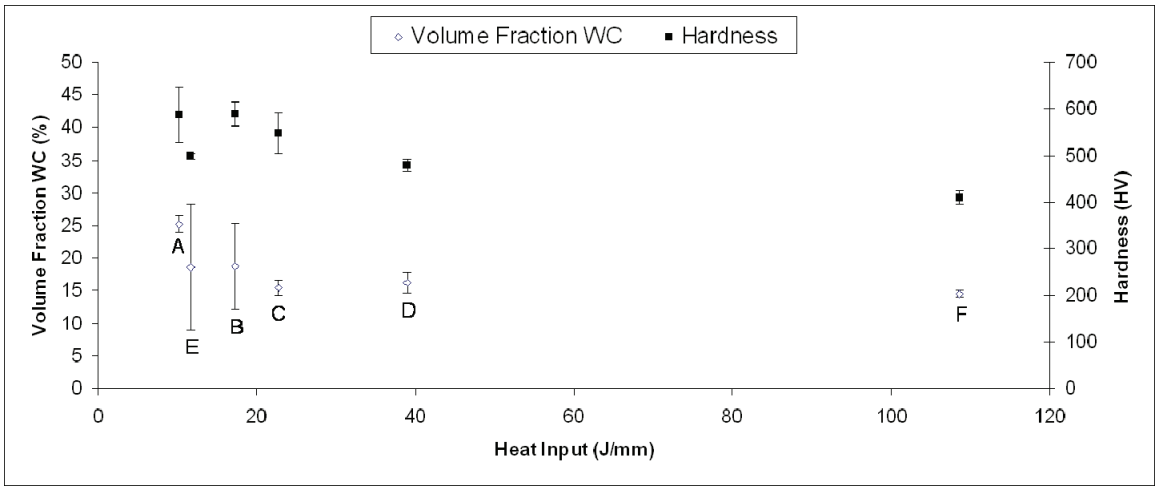

Figure 23: Effect of heat input on the volume fraction and hardness for samples deposited by CSC-MIG

2.4 Conclusions

A commercially available WC/Ni hardfacing electrode wire was deposited by controlled short-circuit (CSC)-MIG welding system. The microstructure of several

hardfacings deposited with different welding parameters and heat inputs were analyzed. Analysis of the welding system and deposited coatings resulted in the following conclusions:

- The CSC-MIG welding system successfully deposited WC/Ni coatings using a hardfacing electrode wire.
- The CSC-MIG welding system can deposit continuous beads free from spatter with 0.75 % average porosity on a carbon steel substrate. Transverse cracking is present.
- The CSC-MIG allows for a high degree of user control over the current waveform and is characterized by heat inputs that are an order of magnitude lower than traditional MIG welding. Heat input for the analyzed coatings ranged from 10.1 J/mm to 108.7 J/mm.
- Many phases and compounds are formed in the weld pool. Phases identified in the hardfacings were: WC, α-W_2C, FeNi, FeW_3C, C, (Fe,C) Ni_3B and $B(Fe,Si)_3$.
- The detrimental decarburization reactions seen in HVOF thermal spraying do not occur with the CSC-MIG welding system.
- The formation of a shell of WC was identified around the mixed WC/W_2C reinforcing phase after welding. The thickness of this shell increased with welding energy from 3.8 μm to 7.2 μm for the low and high heat input conditions, respectively. Isothermal Ni – W – C ternary phase diagrams were used to propose a mechanism for the precipitation of this layer.
- The size distributions of ceramic particles after welding were similar for high and low heat input coatings. The level of WC dissolution increased significantly with heat input.
- Newly formed WC particles precipitated in the Ni-based alloy matrix. Their size distribution increased from D_{50} of 2.4 μm in the low heat input weldment to 6.75 μm in the high heat input weldment.
- The hardness of the deposited coatings decreased from 587 HV_{10} to 410 HV_{10} when the energy input was increased from 10.1 J/mm to 108.7 J/mm.

Chapter 3. CSC-MIG Welding of a Ni-Based Overlay Reinforced with Ultrafine and Nanostructured WC Particles

P. Vespa, P. T. Pinard, R. Gauvin and M. Brochu

Department of Mining and Materials Engineering, McGill University, 3610 University St., Montreal, Quebec, Canada H3A 2B2

3.1 Introduction

Damage caused through wear and corrosion of materials costs the United States hundreds of billions dollars on an annual basis [25]. Research aimed at developing wear resistant materials and coatings can therefore have significant economic benefits. The addition of tungsten carbide (WC) particles within a metallic binder material is a widespread practice used to increase the wear resistance in metal matrix composite (MMC) coatings. In recent years, interest in the use of nanostructured WC in MMCs has increased due to the potential to further increase wear resistance. Research using nanocrystalline WC powders has produced coatings with higher hardness and better abrasion resistance when compared with conventional WC feedstock [91, 92]. The use of a mixture of conventional and nanostructured cemented carbides in laser clad coatings has been shown to reduce wear rates over the use of either one individually [45]. Although the use of WC with small grain sizes show promise in coating deposition techniques, thermal spray systems generally produce nanostructured coatings with lower wear resistance than conventional coatings [75]. This is mainly attributed to high rates of decarburization of the nanocomposite WC powder particles during spraying [63, 75, 93, 94].

The controlled short circuit (CSC)-MIG welding system was developed to overcome certain limitations of traditional MIG welding. It virtually eliminates spatter, has a significantly lower heat input than traditional MIG welding and does not decarburize WC during deposition [15, 17, 95]. In addition, the CSC-MIG welding

system is an economic alternative to HVOF or laser cladding deposition processes; requiring little initial expenditure and is relatively inexpensive to run.

The objective of this work is to study the effects of the conventional, ultrafine and nanostructured WC particle additions to coatings produced by CSC-MIG welding. In this research, the CSC-MIG welding system is used to deposit a WC/Ni hardfacing electrode wire containing conventional sized WC particles. During the welding process, the WC powders are embedded within the coating and the molten metal/particles interface and final crystallite size is examined at high and low heat input conditions.

3.2 Materials and Methods

Tests were conducted using the CSC-MIG welding system manufactured by Jetline Engineering (torch model WF-9829/ weld process controller model 9829). The welder was mounted on a Machitech CNC table and monitored using ARCAgent 3000P data acquisition system by IMPACT Welding.

A 1.6 mm cored electrode wire, PolyTung NiBWC, from Polymet Corporation was used to produce coatings. PolyTung NiBWC is made up of a pure Ni sheath filled with a FeSiB powder and WC particles as a reinforcing agent. Full chemical composition of the cored electrode wire containing 38 – 45 wt. % WC particles, as stated by manufacturer, is shown in Table 1. The angular feedstock WC particle size ranged between 45 – 200 μm in diameter with mean particle diameter of 71 μm.

Table 6: **Chemical composition of starting WC/Ni hardfacing wire.**

Chemical Composition [wt.-%]					
Si	B	Fe	C	W	Ni
0.81	1.06	0.7	2.81	41.02	Balance

The deposited coatings were made using two different conditions. In the first condition, solely the electrode wire was deposited on the plain carbon steel substrate. In the second condition, the electrode wire was deposited in combination with one of three WC powders. During deposition, the electrode wire was traveled through a pre-placed

powder bed; similarly to the submerged arc welding configuration. The first pre-placed WC powder was identical to that used for the filler powder of the electrode wire. The second was manufactured by Alfa Aesar and had a particle size less than 1 um. The third powder embedded was a nanostructured powder manufactured by Inframat which contained 200 nm particles with 40 – 70 nm grain size. The sample names in the present paper are identified by the letters L and H. The letter L is used for the low heat input condition (18 J/mm) and the letter H for the high heat input condition (200 J/mm). In addition, the symbols M, UF and N were used to designate the micron-sized, ultrafine and nanostructured powders, respectively. The morphology of the stock WC powder contained in the electrode wire as well as the ultrafine and nanostructured powders can be seen in Figure 24.

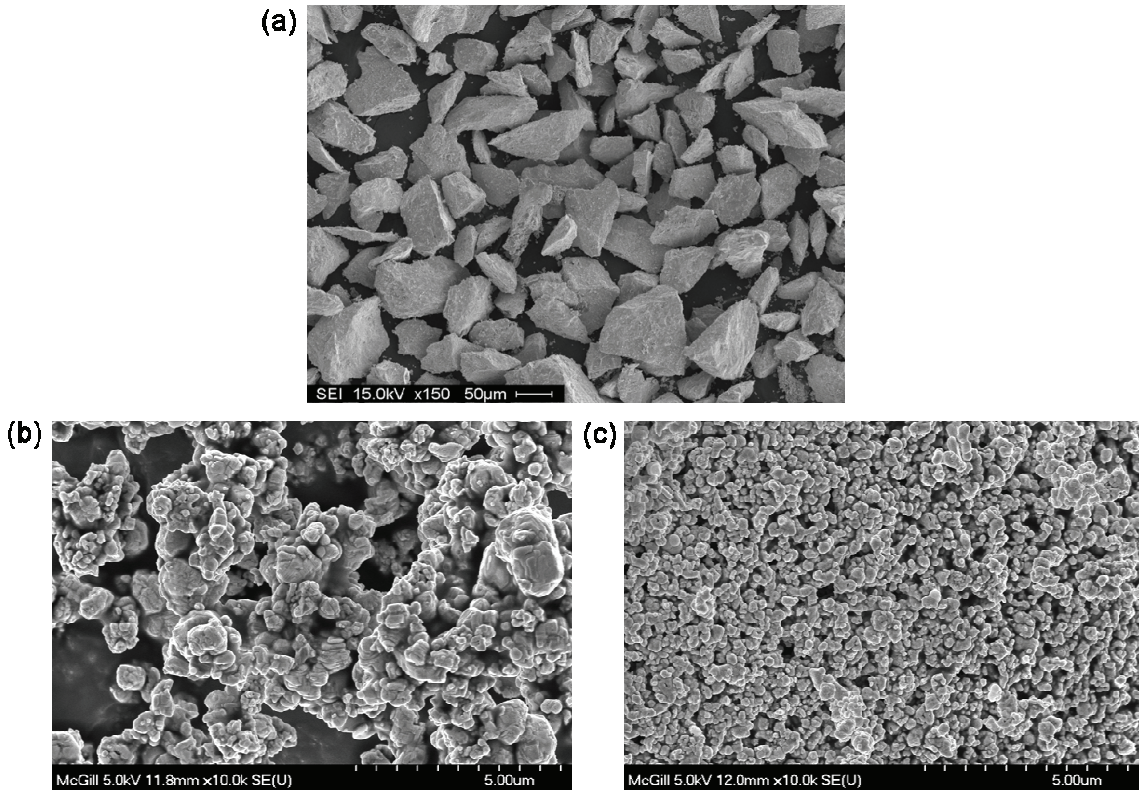

Figure 24: **SEM micrographs of the starting (a) micron-sized, (b) ultrafine and (c) nanostructured WC powders.**

Welding was carried out in the flat position at 1 meter per minute (MPM) on plain carbon steel plates having dimensions of 100 mm x 12 mm x 2.5 mm. The substrates

were sandblasted to remove surface impurities. A plexiglass enclosure was used to maintain a 75Ar –25CO_2 gas environment in the welding area to prevent the shielding gas flow rate from dispersing and/or oxidizing the WC particles. Table 6 lists the CSC-MIG welding process parameters for each welding condition.

Table 7: CSC-MIG welding process parameters and energy input for the reported depositions.

Sample	L-UF / L-NM	H-M / H-UF / H-NM
Heat Input (J/mm)	18.0	200.0
Current Data		
Arc Time		
Initial arc current (A)	30	250
Time (ms)	7	7
Mid arc current (A)	30	250
Time (ms)	7	7
End arc current (A)	30	250
Short Circuit Time		
Start short current (A)	20	200
Time (ms)	7	7
Mid short current (A)	20	200
Time (ms)	7	7
End arc current (A)	20	200
Ramp Rates		
Rise (A/ms)	200	200
Fall (A/ms)	200	200
Wirefeed Data		
Down Wirefeed Speed (mpm)	5	12
Delay Before Wire Down (ms)	0	0
Up 1 Wirefeed Speed (mpm)	5	5
Delay Before Wire up (ms)	0	0
Up 2 Wirefeed Speed (mpm)	7	7
Arc Length (mm)	0.5	0.5
Penetration Delay (ms)	6	6
Start Sequence Data		
Preflow Time (s)	0.5	0.5
Runin Wirefeed Speed (mpm)	2	2
Process Starting Current (A)	60	60
Initial Arc Length (mm)	2	2
Preheat Current (A)	60	60
Preheat Time - Start Delay (ms)	50	50
Stop Sequence Data		
Stop Arc Length (mm)	1.4	1.4
Stop Time (ms)	40	40
Arc Stop Current (A)	40	40
Postflow Time (s)	0.3	0.3
System Data		
Max Arc Time (ms)	4000	4000
Burnfree Current (A)	0	0
Burnfree Delay Time (ms)	100	100
Burnfree Stop Time (ms)	984	984

Scanning electron microscopy (SEM) examination was performed using a JEOL JSM-840A equipped with EDAX Si(Li) EDS. Electron backscattered diffraction (EBSD) analysis was performed on a Hitachi S-4700 cold field emitter equipped with the Nordlys II camera and HKL Channel 5 software. A Bruker D8 Discovery diffractometer using cobalt K_α X-rays at 40 kV and 0.002º step size was used for collecting x-ray diffraction (XRD) patterns.

3.3 Results

3.3.1 Conventional sized WC particles

Research presented in Chapter 2 has shown that WC particles present in the starting electrode wire form a WC reaction layer due to a dissolution/precipitation reaction in WC/Ni coatings deposited by CSC-MIG welding. Analysis showed that the reaction layer thickness is affected by welding energy, shifting the average thickness of the layer from 3.8 μm to 7.6 μm when the heat input is increased from 10.1 J/mm to 108.7 J/mm. However, there is no variation of its thickness between particles located at the edge or at the center of the coating for a given energy input. The increase in reaction layer thickness is caused by the significant rise in temperature of the molten weld pool during the arc transfer which accelerated the dissolution of the reinforcing phase.

To better understand if the pre-placed powder method has an effect on the dissolution behavior, sample H-M, containing micron-sized WC powder particles from the electrode wire as well as those embedded during welding, was analyzed. Figure 25a shows an optical micrograph of sample H-M, taken near the edge of the weldment. As observed, a small reaction layer caused by the dissolution/precipitation phenomenon occurring in the weld pool can be seen on the WC/W_2C particles. The presence of a small reaction layer and preservation of the original particle morphology suggests a small amount of dissolution of WC has occurred. On the other hand, Figure 25b shows a micrograph taken at the center of the coating. In this case, a significantly larger amount of dissolution can be seen in the WC/W_2C reinforcing phase. Figure 25c shows a mosaic of several optical micrographs which highlights the difference in the dissolution of the

WC particles at the edge of the coating to its center. It is evident that the dissolution of the reinforcing carbide varies depending on its location in the weld pool during welding.

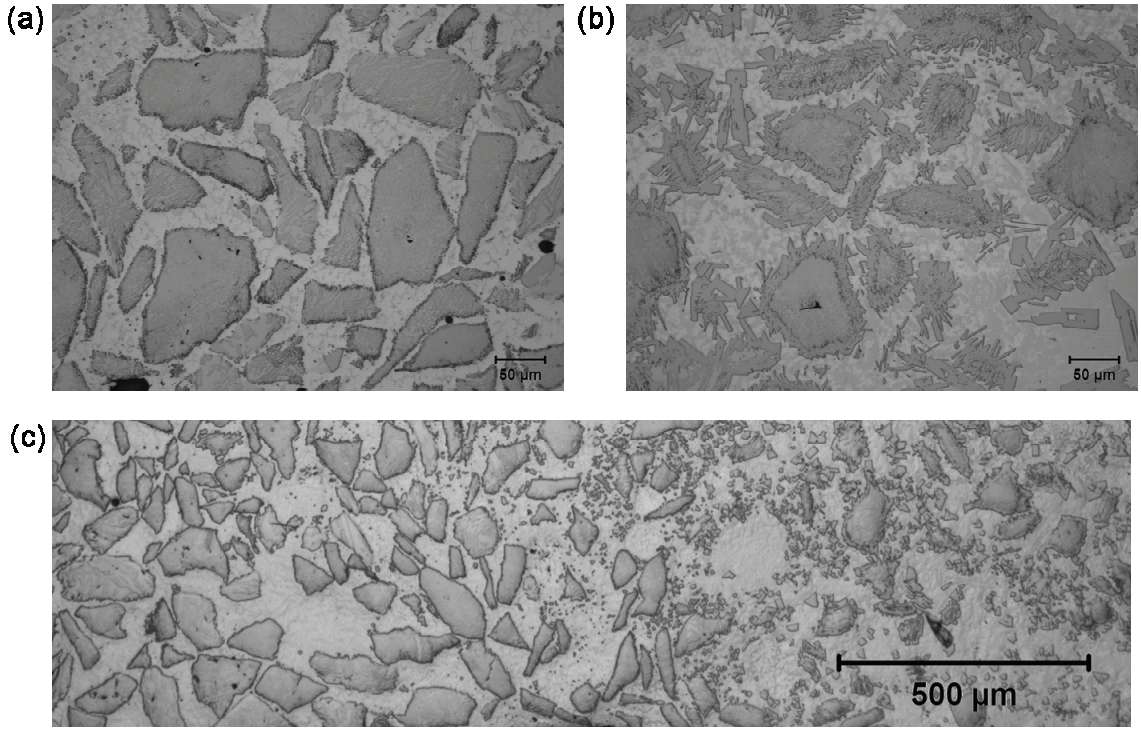

Figure 25: Optical micrographs of high heat input coating, sample H-M, containing micron-sized WC particles from the electrode wire as well as those embedded using the pre-placed powder method. Images (a) and (b) show the reaction layer thickness and quantity of dissolution of the reinforcing phase at the edge and center of the weldment, respectively. Image (c) shows the evolution of the dissolution phenomenon from the edge of weldment towards the center.

3.3.2 Ultrafine WC powder

Figure 26a shows a representative SEM micrograph of the shape of WC particles observed in the L-UF sample. As depicted, the WC particles had a very regular and angular morphology regardless of examination location within the coating. This suggests that the pre-placed ultrafine WC powder completely dissolved within the Ni matrix and precipitated during cooling and solidification of the weldment. EBSD analysis was used to infer the grain structure of the re-precipitated particles as well as their size distribution after welding for the low and high heat input conditions. Figure 26b and 26c show the inverse pole figure representation of the particulates orientation in the Y and Z direction

respectively. The colour code for these crystallographic orientation maps is given in Figure 26d. The lower resolution of the particulates edges in the EBSD maps is due to the topographical changes induced during mechanical polishing. The EBSD results confirm that the ultrafine WC feedstock has re-precipitated as single crystal WC particles, without any preferential orientation. A similar single crystal-based microstructure without any preferential orientation was obtained for the H-UF sample.

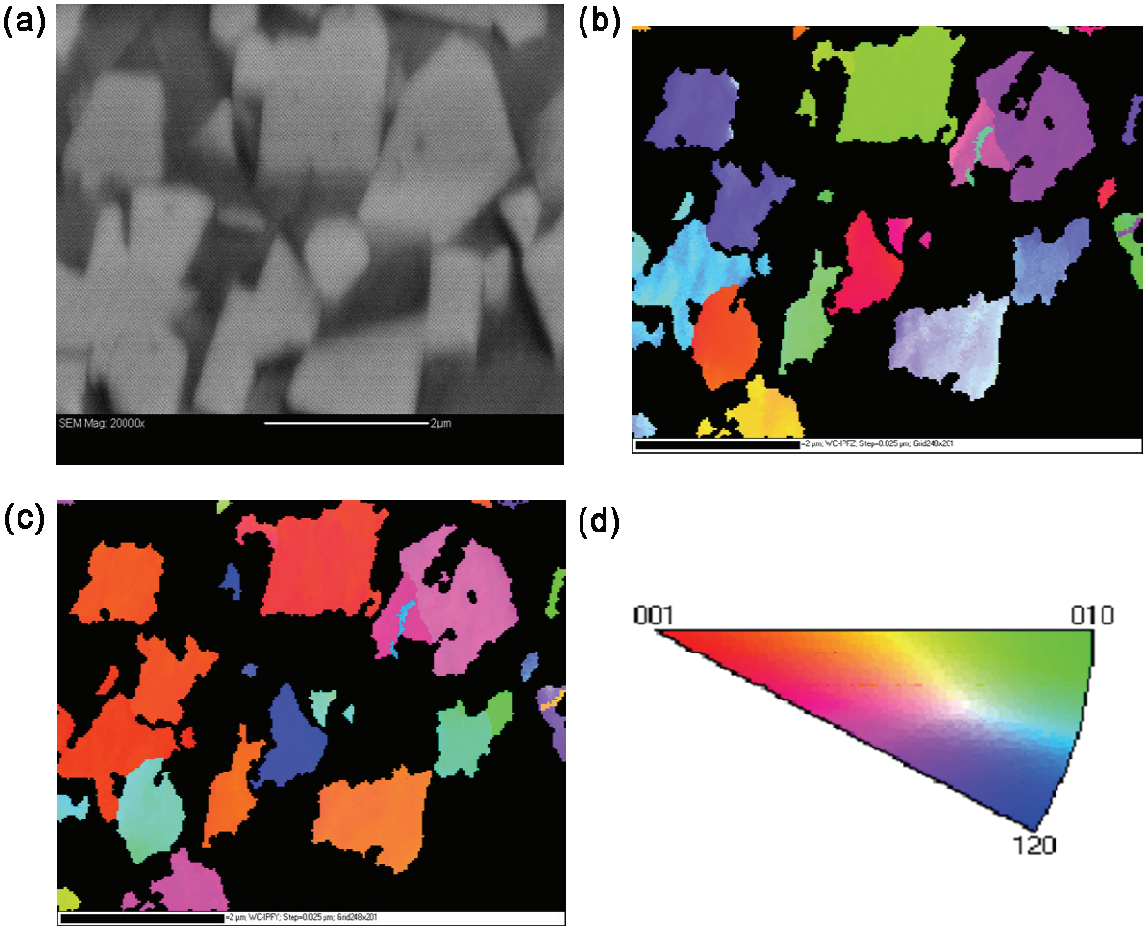

Figure 26: **Images taken of sample L-UF showing: (a) tungsten carbide powder within the nickel matrix; (b-c) Inverse pole figure maps obtained using EBSD showing the orientation of the WC phase with respect to the Y (b) and Z (c) direction; (d) Colour wheel of crystallographic orientation for (b-c). EBSD acquisition was performed at 15 kV using a step size of 25 nm. It should be noted that in the maps, small unindexed regions inside the WC particles were filled in with the orientation of their nearest neighbors.**

Figure 27a and 27b show secondary image SEM micrographs of the L-UF and H-UF samples, respectively. From these micrographs, it is evident that the re-precipitated particle size slightly increases with welding energy. This result is reflected by analysis of

the equivalent spherical particle size distribution, where the average particle size increased from 0.51 μm to 0.60 μm for the low and high heat input conditions, respectively. Similarly, the D_{50} values for the deposition augmented from 0.49 μm for the low heat input condition to 0.56 μm for the high heat input condition. The equivalent spherical particle size diameter distributions of the pre-placed powders after welding are shown in Figure 28 for comparison purposes.

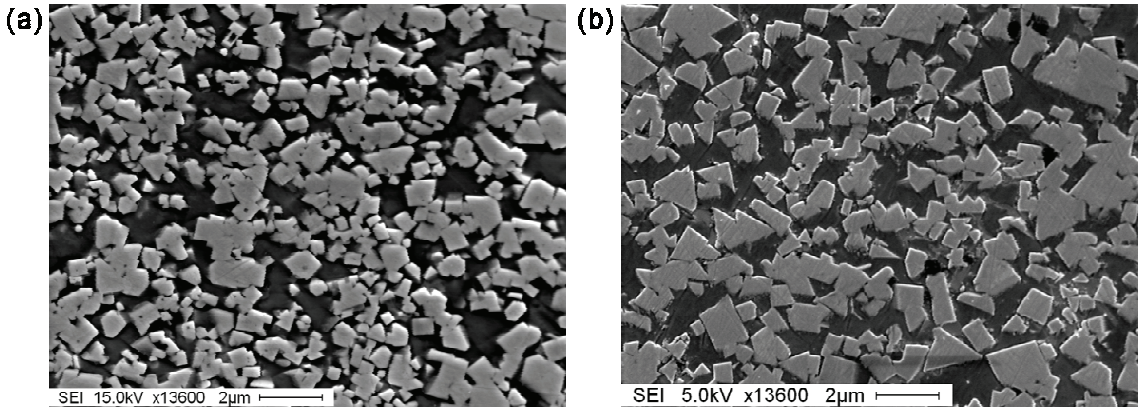

Figure 27: Micrographs of pre-placed WC particles after CSC-MIG welding for (a) low heat input ultrafine (L-UF) and; (b) high heat input ultra-fine (H-UF) coatings.

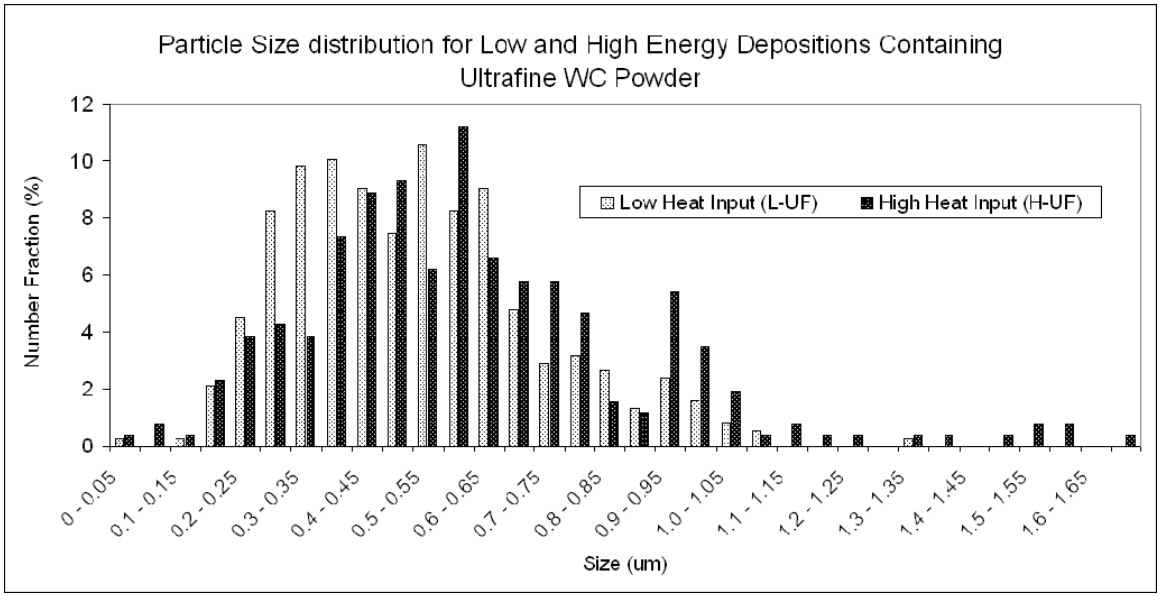

Figure 28: The effect of welding heat input on the final particle size distribution for the low and high heat input conditions with ultrafine WC powder additions.

Figure 29 shows a spectrum overlay of EDS analyses of the Ni-alloy matrix of the ultrafine WC particle (red) and the conventional sized WC particle (brown) specimens. Results show that there is a higher concentration of W in the binder material close to the ultrafine WC particles while its presence in close proximity to the conventional sized particles is minute or inexistent.

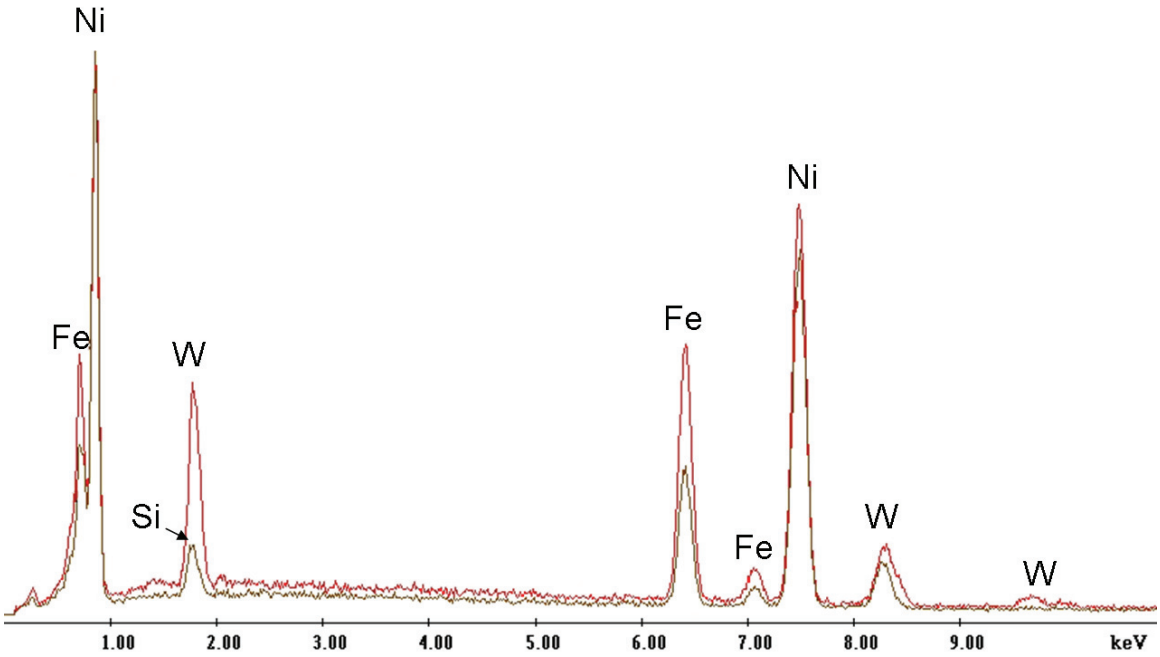

Figure 29: EDS spectrum overlay of the Ni matrix close to and far from the ultrafine WC particle clusters. The scan was conducted at 20 keV and used a live time of 1 minute.

3.3.3 Nanostructured WC powder

Figure 30 shows the XRD spectrums of the stock nanostructured tungsten carbide powder and the high heat input sample H-NS overlaid for the purpose of comparison. From comparison of the full width at half maximum (FWHM) of the largest WC peak before and after welding, it can be seen that there is contraction of the peak. This is a good indication that the nanostructure in the powder is lost during the welding process.

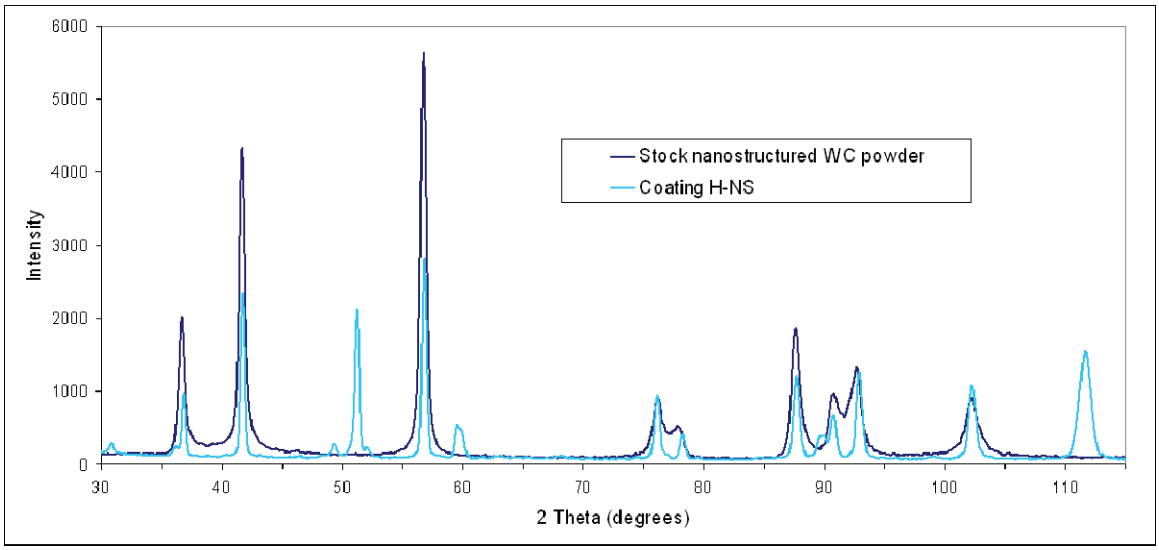

Figure 30: XRD spectrum overlay of the feedstock nanostructured powder and coating H-NS. Broadening of the WC peaks in the coating compared with the feedstock powder shows evidence of the loss of the nanostructure.

As with the ultrafine WC, the nanostructured WC powder dissolved and precipitated throughout both the high and low heat input coatings. Figure 31a and 31b show SEM images of the low and high heat input depositions, respectively. The equivalent spherical particle size distribution analysis reveals that the average diameter for the low heat input condition (18 J/mm) was 0.21 μm while that for the high heat input condition (200 J/mm) was 0.23 μm. Similarly, their size distribution increased from D_{50} = 0.19 μm in the low heat input weldment to D_{50} = 0.21 μm in the high heat input weldment. For the nanostructured powder, the heat input seems to have had a similar effect on the particle size distribution of the low and high heat input conditions. The equivalent spherical particle size diameter distributions of the nanostructured powder after welding for the low and high heat input welding conditions are shown in Figure 32.

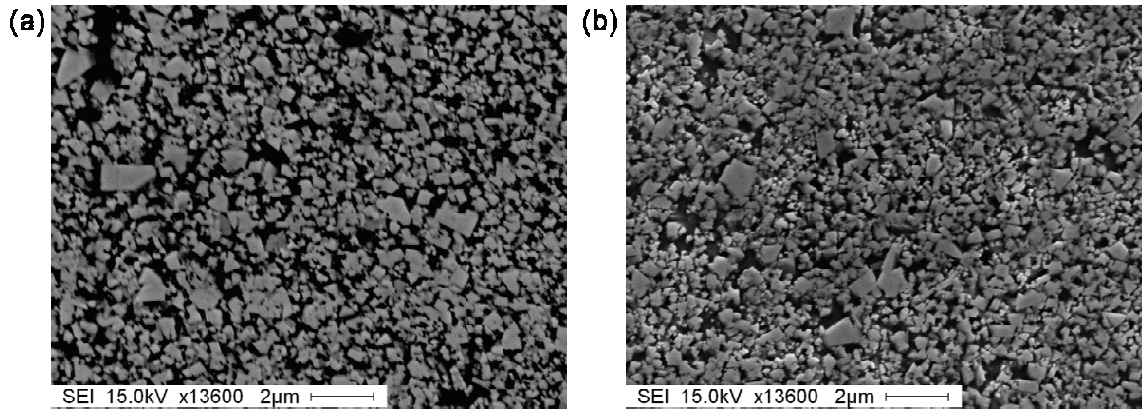

Figure 31: SEM images of: (a) low heat input nanostructured (L-NS) and; (b) high heat input nanostructured (H-NS) coatings.

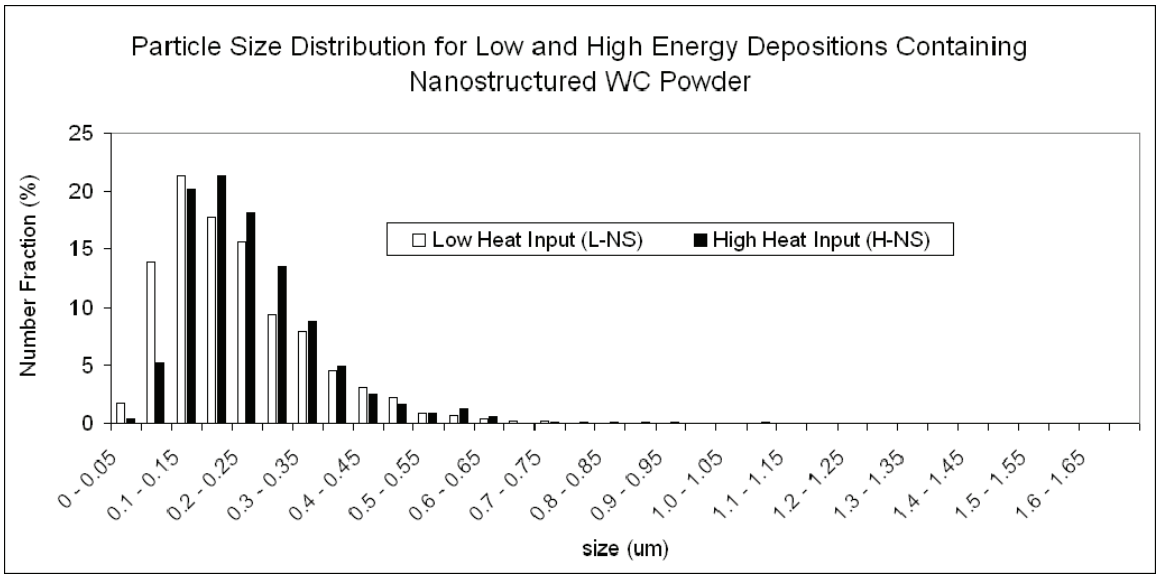

Figure 32: The effect of welding heat input on the nanostructured WC powder particle size distributions for low (L-NS) and high (H-NS) heat input conditions.

3.4 Discussion

The experimental results show that the method of embedding WC feedstock into the coatings deposited by CSC-MIG welding had an effect on the extent of dissolution and the thickness of the precipitated reaction layer on the reinforcing phase. Depositions made using the cored electrode wire containing conventional sized WC powder show a consistent reaction layer thickness throughout the coating for a given heat input [95]. However, when the conventional sized WC feedstock is pre-placed on the substrate and

the electrode wire is deposited through the blanket of WC powder allowing them to be embedded throughout the coating, a difference in the microstructure is observed. The reaction layer thickness on the WC particles is small at the edges of the coating and large in the center. This difference can be explained by the thermal history of the WC particles and thermal gradient in the weld pool. A representative value for the droplet temperature in open arc welding deposition techniques, such as pulsed or spray transfer, has been established at 2400 °C [15]. Given short-circuit welding techniques have significantly lower droplet temperatures, a maximum weld pool temperature (peak temperature) of 2400 °C is a good approximation. Since the coatings have been laid on low carbon steel which has a melting temperature T_m = 1500 °C, the weld pool in contact with the edges of the basemetal is equal to the melting temperature. Although the pre-placed powder particles are not highly affected by the arc, those at the center of the weld pool are affected by the high temperature and long dwell times in the weld pool and therefore show a large reaction layer. On the other hand, the WC particles absorbed by the edges of the weld pool do not reach a temperature much higher than 1500 °C and do not remain at high temperature for a significant amount of time before weld pool solidification. Therefore, the WC particles at the edge of the coating do not show a large reaction layer and are not significantly dissolved.

3.4.1 Dissolution behavior of ultrafine and nanostructured WC powder

The precipitated particles size distribution D_{50} values for the ultrafine and nanostructured coatings can be explained by EDS analysis and by the effect of particle size additions on nucleation rate. The nucleation rate is defined as the total number of particles generated in a certain time during which the supersaturation value remains constant [96, 97]. Its rate depends on both the supersaturation value and the concentration of crystals in suspension which act as active sites for nucleation [98, 99]. The relation between the particle size additions and the quantity of active sites for nucleation has been reported through compositional analysis of conventional and ultrafine powders on Ti(C,N)-xWC-20Ni cermets. Jung and Kang [100] have shown that the binder material can retain up to approximately 45 at.% W solid solution when

ultrafine WC particles are used while the saturation value reached only 25 at.% W for conventional sized particles. This shows that as the particle size decreased, the solid solution saturation value increased. In the current research, EDS analysis of the binder for the ultrafine and conventional coatings revealed a higher concentration of W, or solid solution, in the matrix of the ultrafine coating. Similar to the system studied by Jung and Kang, as the particle size decreases, the solid solution increases. The increase in solid solution is followed by an increase in the number of sites for nucleation in the nanostructured system when compared with the ultrafine system. This results in the precipitation of a finer particle size distribution for the nanostructured powder system.

The precipitated particle size does not vary significantly between the low and high heat input conditions for the ultrafine and nanostructured powder coatings. This can be explained by the fact that the system is so oversaturated with W, the additional dwell time in the molten weld pool for the high heat input condition does not significantly affect the precipitated particle size.

XRD results show that the nanostructure of the WC powder has likely been lost during welding. This is due to the high temperatures associated with arc-welding techniques which caused the dissolution/precipitation reaction. However, the equivalent spherical particle size diameter D_{50} values for the low heat input condition is 210 nm while that for the high heat input condition is 230 nm. These values are approximately equal to the particle size of the original starting powder. It is believed that the precipitation of the ultrafine WC single crystals will improve the mechanical integrity of the WC coatings compared to those without the pre-placed powder.

3.5 Conclusions

The newly developed CSC-MIG welding system has been used to deposit WC-Ni coatings on a plain carbon steel substrate. Either micron-sized, ultrafine or nanostructured WC particles were embedded in the coatings using a pre-placed technique similar to that used for submerged arc welding. The effect of the addition of these powders on the microstructure and dissolution/precipitation behavior has been investigated. Results show:

1) The pre-placed WC powder technique has an effect on the dissolution behavior of conventional sized WC particles. Particles located at the center of the coating underwent significant dissolution while those at the edges remained largely unaffected. Both the ultrafine and nanostructured powders additions underwent a dissolution/precipitation process throughout the high and low heat input coatings.
2) The CSC-MIG welding system has produced coatings with ultrafine and near nano-sized WC particle additions through a dissolution/precipitation reaction. The precipitated particles are single crystals. Analysis of the precipitated particle size distribution for the ultrafine coating resulted in D_{50} = 0.49 μm for the low heat input condition and D_{50} = 0.56 μm for the high heat input condition. The D_{50} values for the nanostructured powder were 0.19 μm and 0.21 μm for the low and high heat input condition, respectively.
3) Although the nanostructure of the nanostructured WC powder is lost during welding, it is believe that the near nano-size WC precipitates will increase the wear resistance compared to the conventional sized WC additions.
4) The solid solution of W in the binder material increases as the particle size is reduced.

Chapter 4. Summary and Future Work

The preceding chapters have shown that the CSC-MIG welding system is a viable option as a coating deposition technique. Chapter 2 has shown that the CSC-MIG allows for a high degree of user control over the current waveform and is capable of depositing continuous beads with a hardfacing electrode wire that are free from spatter, contain a low amount of porosity and are metallurgically bonded to the substrate. When compared with thermal spray deposition techniques, the CSC-MIG is advantageous because it deposits metallurgically bonded coatings with high rates of deposition and which are free from the detrimental decarburization reactions acting on the WC reinforcing phase. Even though the CSC-MIG welding system is characterized by heat inputs which are an order of magnitude lower than traditional MIG welding, high levels of dissolution of the reinforcing phase is a factor which must be contended with. As the hardness of the deposited coatings decreases with energy input, minimizing the heat input during welding through proper parameter selection is required to increase their wear resistance. It was demonstrated that the WC/W_2C particles present in the starting electrode wire form a WC reaction layer due to a dissolution/precipitation reaction. The reaction layer thickness is affected by welding energy, shifting the average thickness of the layer to larger sizes with increasing heat input. It has also been shown that newly formed WC particles are precipitated as single crystals in the Ni-based alloy matrix, the particle size of which also increased with heat input. Research in Chapter 3 showed that ultrafine and near-nanostructured WC particles were capable of being embedded in coatings produced with the CSC-MIG welding system. Analysis revealed that the method of embedding WC particles in the deposited coatings plays a role in the dissolution/precipitation behavior of the reinforcing phase. WC particles located near the external surface of the weldment remain largely unaffected while those at the center of the weldment show greater amounts of dissolution. Coatings deposited using a pre-placed method containing ultrafine and nanostructured WC particles have been shown to precipitate newly formed WC particles as single crystals. The presence of ultrafine and near nano-size WC precipitates is expected to increase the wear resistant properties of the deposited coatings.

The CSC-MIG welding system is in the preliminary phases of research as a WC/Ni deposition technique. Future work with the cladding system can take several directions. Firstly, quantification of the wear resistance of deposited coatings containing conventional, ultrafine and/or nanostructured WC particles would provide insight into the tribological properties of the deposited coatings and allow for better comparison with other deposition techniques. Secondly, deposition of coatings on mechanical parts and conducting tests under real industrial settings would provide insight as to how the working conditions affect the hardfacings and their wear life. In addition, analysis and comparison of the microstructure of deposited coatings from CSC-MIG with traditional MIG welding would provide information as to the difference in the effect of each welding system on wear resistance and the dissolution of WC particles. This comparison would also allow for better understanding of the effect of the welding parameters on the deposited coatings.

References

1. Messler, R.W., *Joining of materials and structures : from pragmatic process to enabling technology*. 2004, Amsterdam ; Boston :: Elsevier.

2. Norrish, J., *Advanced welding processes : technologies and process control*. Woodhead Publishing in materials. 2006, Cambridge :: Woodhead Pub. : Maney Pub.

3. Callister, W.D., *Materials science and engineering : an introduction*. 2007, New York :: John Wiley & Sons.

4. Sacks, R.J., *Welding, principles and practices*. 1976, Peoria, Ill. :: C. A. Bennett Co.

5. Naidu, D.S., S. Ozcelik, and K.L. Moore, *Modeling, sensing and control of gas metal arc welding*. 2003, Amsterdam : London :: Elsevier.

6. Raj, B., V. Shankar, and A.K. Bhaduri, *Welding technology for engineers*. 2006, Oxford :: Alpha Science International.

7. International, A.S.M., *ASM handbook*. Vol. 6. 1990, Materials Park, OH :: ASM International.

8. Kou, S., *Welding metallurgy*. 2003, Hoboken, N.J. :: Wiley-Interscience.

9. Ghosh, P.K., et al., *Arc characteristics and behaviour of metal transfer in pulsed current GMA welding of stainless steel.* Journal of Materials Processing Technology. **In Press, Corrected Proof**.

10. P. Praveen, P.K.D.V.Y., *Pulsed Gas Metal Arc Welding (GMAW-P) for Newer Challenges in Welding of Aluminum Alloys*. 2005.

11. Modenesi, P.J. and R.C. de Avelar, *The influence of small variations of wire characteristics on gas metal arc welding process stability.* Journal of Materials Processing Technology, 1998. **86**(1-3): p. 226-232.

12. Palani, P.K. and N. Murugan, *Selection of parameters of pulsed current gas metal arc welding.* Journal of Materials Processing Technology, 2006. **172**(1): p. 1-10.

13. Ahmed, N., *New developments in advanced welding*. Woodhead Publishing in materials. 2005, Boca Raton, FL : Cambridge, England :: CRC Press ; Woodhead Pub.

14. Praveen, P., M.J. Kang, and P.K.D.V. Yarlagadda, *Drop transfer mode prediction in pulse GMAW of aluminum using statistical model.* Journal of Materials Processing Technology, 2008. **201**(1-3): p. 502-506.

15. Huismann, G., Hoffmeister, H., *Control of the Short Circuiting MIG-Process Under Hyperbaric Conditions.* OMAE, 1998.

16. Suban, M. and J. Tusek, *Methods for the determination of arc stability.* Journal of Materials Processing Technology, 2003. **143-144**: p. 430-437.

17. Huismann, G., *Direct control of the material transfer: the controlled short circuiting (CSC)-MIG process.* Proceedings of the gas metal arc wedling for 21st century conference (American Welding Society), 2000: p. 165-172.

18. *Jetline Engineering - Product Information (CSC MIG Weld Process Controller)*. [cited.

19. Lu, M., and Kou, W., *Weld.* 1989: p. 452s, 382s.

20. Feng, Z., *Processes and mechanisms of welding residual stress and distortion*. Woodhead Publishing in materials. 2005, Boca Raton, Fla. :: CRC Press.

21. Deyev, G.F. and D.G. Deyev, *Surface phenomena in fusion welding processes*. 2006, Boca Raton, FL :: CRC Taylor & Francis.

22. Stewart, J.P., *Welder's troubleshooting guide*. 1983, Reston, Va. :: Reston Pub. Co.

23. Yiu Wing, C., *Computer simulation of heat flow in pulsed current arc welding.* Journal of Materials Processing Technology, 1993. **38**(1-2): p. 449-463.

24. Chattopadhyay, R., *Surface wear : analysis, treatment, and prevention*. 2001, Materials Park, OH :: ASM International.

25. *Surface Engineering for Corrosion and Wear Resistance*, in *ASM Handbook*. 2001, ASM International.

26. Callister, W.D., *Materials science and engineering : an introduction*. 2000, New York: Wiley.

27. Zhou, S. and X. Dai, *Laser induction hybrid rapid cladding of WC particles reinforced NiCrBSi composite coatings.* Applied Surface Science, 2010. **In Press, Corrected Proof**.

28. Nurminen, J., J. Näkki, and P. Vuoristo, *Microstructure and properties of hard and wear resistant MMC coatings deposited by laser cladding.* International Journal of Refractory Metals and Hard Materials, 2009. **27**(2): p. 472-478.

29. Zhou, S., Y. Huang, and X. Zeng, *A study of Ni-based WC composite coatings by laser induction hybrid rapid cladding with elliptical spot.* Applied Surface Science, 2008. **254**(10): p. 3110-3119.

30. Sari, N.Y. and M. Yilmaz, *Improvement of wear resistance of wire drawing rolls with Cr-Ni-B-Si + WC thermal spraying powders.* Surface and Coatings Technology, 2008. **202**(13): p. 3136-3141.

31. Witkin, D.B. and E.J. Lavernia, *Synthesis and mechanical behavior of nanostructured materials via cryomilling.* Progress in Materials Science, 2006. **51**(1): p. 1-60.

32. Tobar, M.J., et al., *Morphology and characterization of laser clad composite NiCrBSi-WC coatings on stainless steel.* Surface and Coatings Technology, 2006. **200**(22-23): p. 6313-6317.

33. Van Acker, K., et al., *Influence of tungsten carbide particle size and distribution on the wear resistance of laser clad WC/Ni coatings.* Wear, 2005. **258**(1-4): p. 194-202.

34. Badisch, E. and M. Kirchgaßner, *Influence of welding parameters on microstructure and wear behaviour of a typical NiCrBSi hardfacing alloy reinforced with tungsten carbide.* Surface and Coatings Technology, 2008. **202**(24): p. 6016-6022.

35. Stachowiak, G.B. and G.W. Stachowiak, *Tribological characteristics of WC-based claddings using a ball-cratering method.* International Journal of Refractory Metals and Hard Materials. **28**(1): p. 95-105.

36. Bhushan, B., *Introduction to tribology*. 2002, New York :: John Wiley & Sons.

37. Upadhyaya, G.S. and Knovel, *Cemented tungsten carbides production, properties, and testing*. Materials science and process technology series. Ceramic and other materials--processing and technology. 1998, Westwood, N.J. :: Noyes Publications.

38. Hoa, S.V. and Knovel, *Principles of the manufacturing of composite materials*. 2009, Lancaster, PA :: DEStech Publications, Inc.

39. Krishna, B.V., et al., *Microstructure and properties of flame sprayed tungsten carbide coatings.* International Journal of Refractory Metals and Hard Materials, 2002. **20**(5-6): p. 355-374.

40. Schwetzke, R. and H. Kreye, *Microstructure and properties of tungsten carbide coatings sprayed with various high-velocity oxygen fuel spray systems.* Journal of Thermal Spray Technology, 1999. **8**(3): p. 433-439.

41. Just, C., E. Badisch, and J. Wosik, *Influence of welding current on carbide/matrix interface properties in MMCs.* Journal of Materials Processing Technology. **210**(2): p. 408-414.

42. Wang, Q., Z.H. Chen, and Z.X. Ding, *Performance of abrasive wear of WC-12Co coatings sprayed by HVOF.* Tribology International, 2009. **42**(7): p. 1046-1051.

43. O'Quigley, D.G.F., S. Luyckx, and M.N. James, *An empirical ranking of a wide range of WC-Co grades in terms of their abrasion resistance measured by the ASTM standard B 611-85 test.* International Journal of Refractory Metals and Hard Materials, 1997. **15**(1-3): p. 73-79.

44. Neville, A., et al., *Erosion-corrosion behaviour of WC-based MMCs in liquid-solid slurries.* Wear. **259**(1-6): p. 181-195.

45. Chen, H., et al., *Sliding wear behaviour of laser clad coatings based upon a nickel-based self-fluxing alloy co-deposited with conventional and nanostructured tungsten carbide-cobalt hardmetals.* Wear. **259**(7-12): p. 801-806.

46. Lu, S.-P., O.-Y. Kwon, and Y. Guo, *Wear behavior of brazed WC/NiCrBSi(Co) composite coatings.* Wear, 2003. **254**(5-6): p. 421-428.

47. Dent, A., S. DePalo, and S. Sampath, *Examination of the wear properties of HVOF sprayed nanostructured and conventional WC-Co cermets with different binder phase contents.* Journal of Thermal Spray Technology, 2002. **11**(4): p. 551-558.

48. Li, C.J., A. Ohmori, and Y. Harada, *Effect of powder structure on the structure of thermally sprayed WC-Co coatings.* Journal of Materials Science, 1996. **31**(3): p. 785-794.

49. Amado, J.M., et al., *Laser cladding of tungsten carbides (Spherotene®) hardfacing alloys for the mining and mineral industry.* Applied Surface Science, 2009. **255**(10): p. 5553-5556.

50. Grigorescu, I.C., et al., *Phase characterization in Ni alloy-hard carbide composites for fused coatings.* Surface and Coatings Technology, 1995. **76-77**(Part 2): p. 494-498.

51. Kear, B., et al., *Thermal sprayed nanostructured WC/Co hardcoatings.* Journal of Thermal Spray Technology, 2000. **9**(3): p. 399-406.

52. Grimberg, I., et al., *Tungsten carbide coatings deposited by high-velocity oxy-fuel spraying on a metallized polymeric substrate.* Surface and Coatings Technology, 1997. **90**(1-2): p. 82-90.

53. Li, Q., T.C. Lei, and W.Z. Chen, *Microstructural characterization of WCp reinforced Ni-Cr-B-Si-C composite coatings.* Surface and Coatings Technology, 1999. **114**(2-3): p. 285-291.

54. Zhou, S., et al., *Microstructure characteristics of Ni-based WC composite coatings by laser induction hybrid rapid cladding.* Materials Science and Engineering: A, 2008. **480**(1-2): p. 564-572.

55. Lu, S.-P. and O.-Y. Kwon, *Microstructure and bonding strength of WC reinforced Ni-base alloy brazed composite coating.* Surface and Coatings Technology, 2002. **153**(1): p. 40-48.

56. Zhou, S., et al., *Analysis of crack behavior for Ni-based WC composite coatings by laser cladding and crack-free realization.* Applied Surface Science, 2008. **255**(5, Part 1): p. 1646-1653.

57. Iordachescu, D., et al., *Influence of shielding gases and process parameters on metal transfer and bead shape in MIG brazed joints of the thin zinc coated steel plates.* Materials & Design, 2006. **27**(5): p. 381-390.

58. Huang, S.W., D. Nolan, and M. Brandt, *Pre-placed WC/Ni clad layers produced with a pulsed Nd:YAG laser via optical fibres.* Surface and Coatings Technology, 2003. **165**(1): p. 26-34.

59. Klimpel, A., et al., *The study of properties of Ni-WC wires surfaced deposits.* Journal of Materials Processing Technology, 2005. **164-165**: p. 1046-1055.

60. Kear, B.H., G. Skandan, and R.K. Sadangi, *Factors controlling decarburization in HVOF sprayed nano-WC/Co hardcoatings.* Scripta Materialia, 2001. **44**(8-9): p. 1703-1707.

61. Guilemany, J.M., et al., *Microstructure characterization of WC-Ni coatings obtained by HVOF thermal spraying.* Scripta Metallurgica et Materialia, 1995. **33**(1): p. 55-61.

62. Thorpe, M. and H. Richter, *A pragmatic analysis and comparison of HVOF processes.* Journal of Thermal Spray Technology, 1992. **1**(2): p. 161-170.

63. Qiao, Y., T.E. Fischer, and A. Dent, *The effects of fuel chemistry and feedstock powder structure on the mechanical and tribological properties of HVOF thermal-sprayed WC-Co coatings with very fine structures.* Surface and Coatings Technology, 2003. **172**(1): p. 24-41.

64. Guilemany, J., et al., *Characterization of the W2C phase formed during the high velocity oxygen fuel spraying of a WC + 12 pct Co powder.* Metallurgical and Materials Transactions A, 1999. **30**(8): p. 1913-1921.

65. R. Knight, R.W.S., *ASM Handbook - Thermal Spray Forming of Materials*. Powder Metal Technologies and Applications. Vol. 7. 1998: ASM International.

66. Hazzard, R., *Surface coatings 2--Arc-welded coatings.* Tribology, 1972. **5**(5): p. 207-214.

67. Fernandes, C.M., et al., *Carbide phases formed in WC-M (M = Fe/Ni/Cr) systems.* Ceramics International, 2009. **35**(1): p. 369-372.

68. Cao, G. and Knovel, *Nanostructures & nanomaterials synthesis, properties & applications*. Nanostructures and nanomaterials. 2004, London :: Imperial College Press.

69. Hornyak, G.L., *Introduction to nanoscience*. 2008, Boca Raton :: CRC Press.

70. Edelstein, A.S. and R.C. Cammarata, *Nanomaterials : synthesis, properties, and applications*. 1996, Bristol; Philadelphia: Institute of Physics Pub.

71. Geckeler, K.E. and E. Rosenberg, *Functional nanomaterials*. Nanotechnology book series ; 10. 2006, Stevenson Ranch, Calif. :: American Scientific Publishers.

72. Suryanarayana, C., *Structure and properties of nanocrystalline materials.* Bulletin of Materials Science, 1994. **17**(4): p. 307-346.

73. Suryanarayana, C. and C.C. Koch, *Nanocrystalline materials – Current research and future directions.* Hyperfine Interactions, 2000. **130**(1): p. 5-44.

74. Guilemany, J.M., S. Dosta, and J.R. Miguel, *The enhancement of the properties of WC-Co HVOF coatings through the use of nanostructured and microstructured feedstock powders.* Surface and Coatings Technology, 2006. **201**(3-4): p. 1180-1190.

75. Guilemany, J.M., et al., *Study of the Properties of WC-Co Nanostructured Coatings Sprayed by High-Velocity Oxyfuel.* Journal of Thermal Spray Technology, 2005. **14**: p. 405-413.

76. Zhu, Y.-c., et al., *Tribological properties of nanostructured and conventional WC-Co coatings deposited by plasma spraying.* Thin Solid Films, 2001. **388**(1-2): p. 277-282.

77. H. J. Scussel, G.V., *ASM Handbook - Friction and Wear of Cemented Carbides*. Friction, Lubrication, and Wear Technology. Vol. 18. 1992: ASM International.

78. Przybylowicz, J. and J. Kusinski, *Structure of laser cladded tungsten carbide composite coatings.* Journal of Materials Processing Technology, 2001. **109**(1-2): p. 154-160.

79. Lima, R.S., et al., *Microstructural characteristics of cold-sprayed nanostructured WC-Co coatings.* Thin Solid Films, 2002. **416**(1-2): p. 129-135.

80. A. Joseph, D.H., D. F. Farson, R. Richardson, *Measurement and calculation of arc power and heat transfer efficiency in pulsed gas metal arc welding.* Science and technology of welding and joining 2003. **8**(6): p. 400 - 406.

81. Joseph, A., et al., *Influence of GMAW-P current waveforms on heat input and weld bead shape.* Science & Technology of Welding & Joining, 2005. **10**(3): p. 311-318.

82. Bosworth, M.R., *Effective Heat Input in Pulsed Current Gas Metal Arc-Welding with Solid Wire Electrodes.* Welding Journal, 1991. **70**(5 May): p. S111-S117.

83. Miyaki, M., *Process for the Production of Tungsten Carbide or Mixed Metal Carbides*, U.S. Patent, Editor. 1977: U.S.A.

84. Terry, C.J., *Macrocrystalline Tungsten Monocarbide Carbide Powder and Process for Producing*, U.S. Patent, Editor. 1989: U.S.A.

85. Scotti, A. and L.A. Albuquerque Rosa, *Influence of oscillation parameters on crack formation in automatic Fe---B hardfacing.* Journal of Materials Processing Technology, 1997. **65**(1-3): p. 272-280.

86. Abbas, G. and D.R.F. West, *Laser surface cladding of stellite and stellite-SiC composite deposits for enhanced hardness and wear.* Wear, 1991. **143**(2): p. 353-363.

87. Knotek, O., H. Reimann, and P. Lohage, *Reactions between NiCrBSi matrixes and cabride additives in coatings during treatment.* Thin Solid Films, 1981. **83**(3): p. 361-367.

88. Levashov, E.A., et al., *Structure and properties of dispersion-strengthened-with-nanosized particles refractory hard material TiC-Ni-alloy.* Science and Technology of Advanced Materials, 2003. **4**(3): p. 221-228.

89. P.Gustafson, A.G., I.Ansara, Z.Metallkde, 1986. **78**: p. 151-156.

90. Gupta, D. and L. Seigle, *Free energies of formation of WC and W2C, and the thermodynamic properties of carbon in solid tungsten.* Metallurgical and Materials Transactions A, 1975. **6**(10): p. 1939-1944.

91. Fischer, T.E. and K. Jia, *Abrasion resistance of nanostructured and conventional cemented carbides.* Wear, 1996. **200**(1-2): p. 206-214.

92. Jia, K. and T.E. Fischer, *Sliding wear of conventional and nanostructured cemented carbides.* Wear, 1997. **203-204**: p. 310-318.

93. Shipway, P.H., D.G. McCartney, and T. Sudaprasert, *Sliding wear behaviour of conventional and nanostructured HVOF sprayed WC-Co coatings.* Wear. **259**(7-12): p. 820-827.

94. Stewart, D.A., P.H. Shipway, and D.G. McCartney, *Abrasive wear behaviour of conventional and nanocomposite HVOF-sprayed WC-Co coatings.* Wear, 1999. **225-229**(Part 2): p. 789-798.

95. P. Vespa, P. T. Pinard., R. Gauvin, M. Brochu,, *Analysis of WC/Ni Based Coatings Deposited by Controlled Short-Circuit MIG Welding* Journal of Materials Engineering and Performance.

96. Dirksen, J.A. and T.A. Ring, *Fundamentals of crystallization: Kinetic effects on particle size distributions and morphology.* Chemical Engineering Science, 1991. **46**(10): p. 2389-2427.

97. Mersmann, A., *Crystallization technology handbook*. 1995, New York :: M. Dekker.

98. Mullin, J.W., *Crystallization*. 2001, Oxford ; Boston :: Butterworth-Heinemann.

99. Garside, J., et al., *Measurement of crystal growth and nucleation rates*. 2002, Rugby :: Institution of Chemical Engineers.

100. Jung, J. and S. Kang, *Effect of ultra-fine powders on the microstructure of Ti(CN)-xWC-Ni cermets.* Acta Materialia, 2004. **52**(6): p. 1379-1386.